Projective Visual Hulls

Svetlana Lazebnik[1] (slazebni@uiuc.edu)
Yasutaka Furukawa[1] (yfurukaw@uiuc.edu)
Jean Ponce[1,2] (jponce@uiuc.edu)
[1] *Department of Computer Science and Beckman Institute*
University Of Illinois, Urbana, IL 61801, USA
[2] *Département d'Informatique*
Ecole Normale Supérieure, Paris, France

Abstract. This article presents a novel method for computing the visual hull of a solid bounded by a smooth surface and observed by a finite set of cameras. The visual hull is the intersection of the visual cones formed by back-projecting the silhouettes found in the corresponding images. We characterize its surface as a generalized polyhedron whose faces are visual cone patches; edges are *intersection curves* between two viewing cones; and vertices are *frontier points* where the intersection of two cones is singular, or *intersection points* where triples of cones meet. We use the mathematical framework of *oriented projective differential geometry* to develop an image-based algorithm for computing the visual hull. This algorithm works in a weakly calibrated setting—that is, it only requires projective camera matrices or, equivalently, fundamental matrices for each pair of cameras. The promise of the proposed algorithm is demonstrated with experiments on several challenging data sets and a comparison to another state-of-the-art method.

Keywords: Silhouette, visual hull, frontier point, projective differential geometry, oriented projective geometry, projective reconstruction, 3D photography.

1. Introduction

This article addresses the problem of computing the *visual hull* of a solid object bounded by a smooth closed surface and observed by a finite number of pinhole cameras. The visual hull is defined as the maximal volume consistent with an object's silhouettes as seen from some set of viewpoints (Laurentini, 1994), and can be obtained by intersecting the solid *visual cones* formed by back-projecting the object's silhouettes found in each camera's image plane (Figure 1). The idea of approximating an object's shape as an intersection of visual cones has existed for over three decades, dating back to Baumgart (1974), and it continues to be widely used today as a basis for many approaches to *3D photography*, or

the acquisition of high-quality geometric and photometric models of complex real-world objects — see (Hernández Esteban and Schmitt, 2004; Furukawa and Ponce, 2006; Matusik et al., 2002; Sinha and Pollefeys, 2005; Vogiatzis et al., 2005) for a few recent examples. However, despite the computer vision community's long-standing familiarity with the concept of the visual hull, the issue of computing its intrinsic combinatorial and topological structure has received relatively little attention. Most existing visual cone intersection algorithms produce generic volumetric or polygonal representations of their output, whereas we argue in this article that the visual hull is much more naturally described as a *generalized polyhedron* (Hoffmann, 1989) whose *faces* are patches belonging to surfaces of individual visual cones, *edges* are segments of *intersection curves* of pairs of cone surfaces, and *vertices* are isolated points of contact of three or more faces. Equivalently, the boundary of the visual hull can be described as a union of *cone strips* belonging to the surfaces of individual cones (Figure 2).

This article presents an algorithm for computing the boundary of the visual hull by taking advantage of its *intrinsically projective* structure determined by special kinds of *contacts* between visual rays and the object's surface in 3D. (It is well known that such contacts are the domain of projective geometry, and are preserved under all smooth transformations that map lines to lines.) In particular, as we will show in Section 4, the vertices of the visual hull are of two types, corresponding to two different types of contacts. The first vertex type, illustrated in Figure 3(a), is a *frontier point* where visual rays from two different cameras are simultaneously tangent to the object's surface. A frontier point is a singularity of an intersection curve between two cones where the two corresponding strips cross each other (Figure 2). The second vertex type, illustrated in Figure 3(b), is an *intersection point* where visual rays from three different cameras meet in space after touching the surface of the object at three different locations. As seen in Figure 2, three cone strips meet at each intersection point.

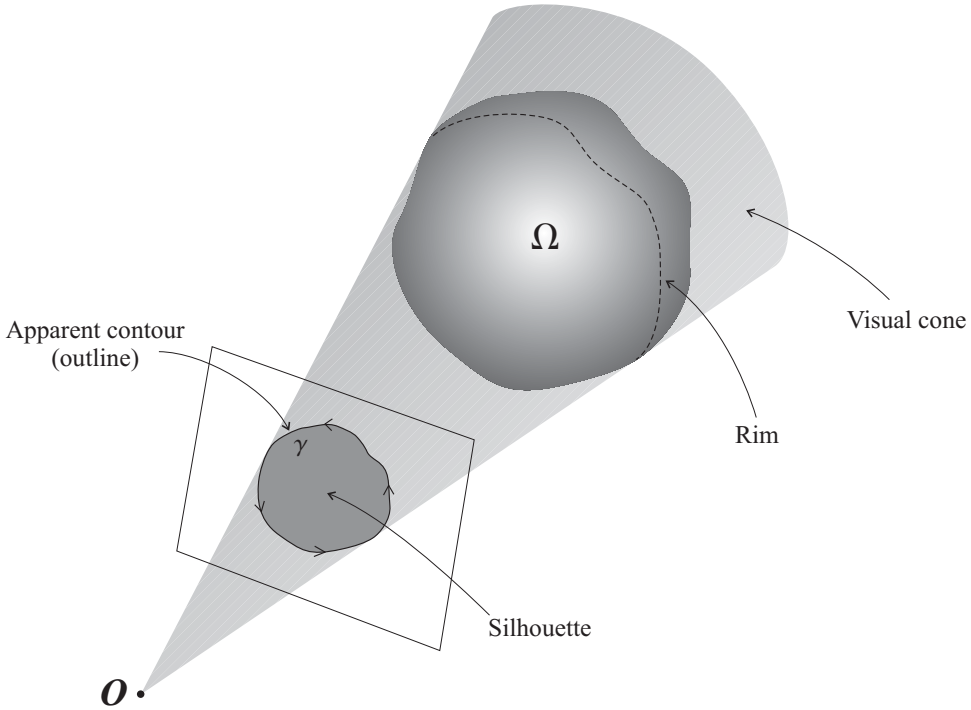

Figure 1. A solid object Ω is observed by a camera with center O. The *visual cone* due to this camera is formed by back-projecting the *silhouette* of Ω seen in the camera's image plane. The boundary of the silhouette in the image is the *apparent contour* or the *outline* γ. Note that γ is oriented such that the silhouette is on its left side (Section 3.2). The surface of the visual cone grazes the object along a curve called the *rim*.

Even though purely projective properties are sufficient to characterize the vertices of the visual hull, they are insufficient to obtain a complete combinatorial description of the visual hull boundary. In standard projective geometry, it is impossible to define a half-line or a segment, and intuitive relations such as front or back have no meaning. In the present article, we overcome this difficulty by adopting an *oriented* extension of projective geometry (Stolfi, 1991). More specifically, we follow the framework of *oriented projective differential geometry* (Lazebnik, 2002; Lazebnik and Ponce, 2005), which gives us the most elementary mathematical machinery sufficient for computing the visual hull. In particular, it does not require cameras to be strongly calibrated and works when only the fundamental matrices between pairs of cameras are known. Our method is completely *image-based*, i.e., it does not perform any 3D computations such as intersections of polyhedra in space. Unlike most existing approaches, ours

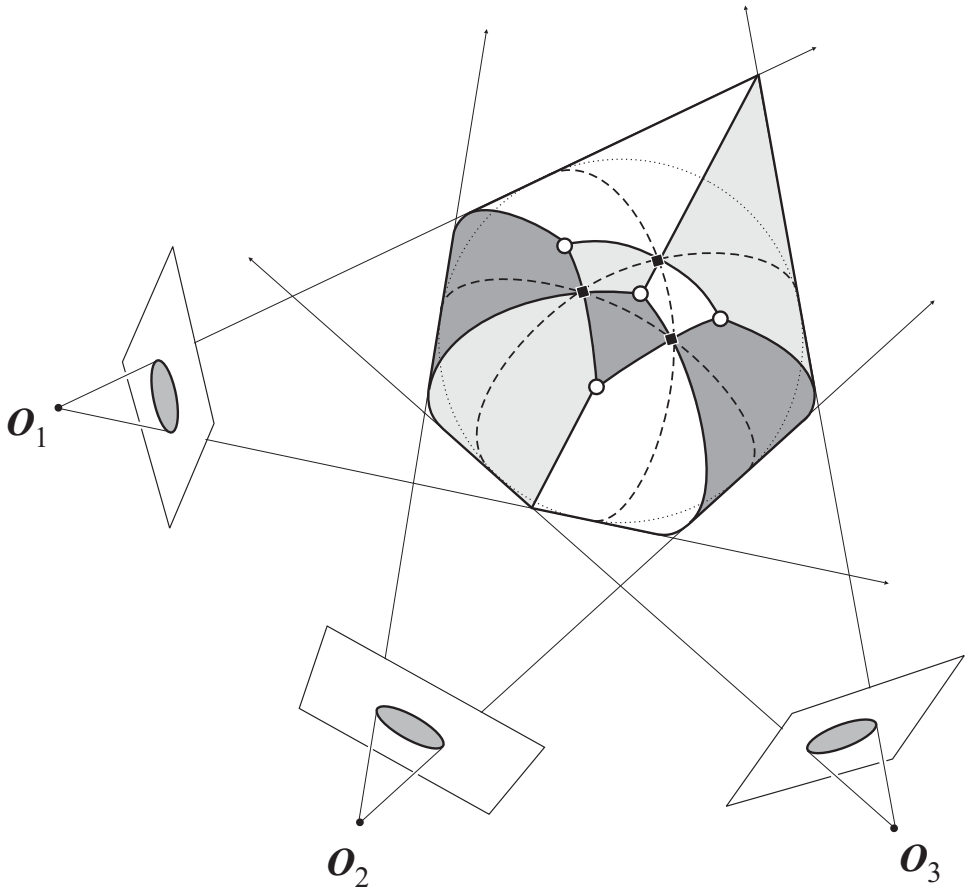

Figure 2. Toy example of visual hull construction. Three cameras with centers O_1, O_2, and O_3 are observing a spherical object. The three visual cones formed by back-projecting the silhouettes graze the surface of the object along the three dashed *rims*. The visual hull surface is made up of three *cone strips*, indicated by three different shades (white corresponds to the first cone strip, dark gray to the second one, and light gray to the third one). As will be discussed in Section 4, vertices of the visual hull are of two types: *frontier points* (shown as black diamonds) where two strips cross each other, and *intersection points* (shown as white circles) where three strips meet. Note that frontier points also correspond to pairwise intersections of rims — an important geometric fact that will be discussed in detail in Section 4.1.

produces a representation of the visual hull in terms of its *intrinsic projective features* (i.e., frontier points, intersection points, and intersection curve segments), instead of artifacts of discretization like polygons, voxels, or irregularly sampled points.

The rest of the article is organized as follows. Section 2 discusses related work, and Section 3 lists the key mathematical machinery and notation used in our presentation. Section 4 describes the proposed algorithm for visual hull construction. Along the way, we state several theoretical results (Propositions

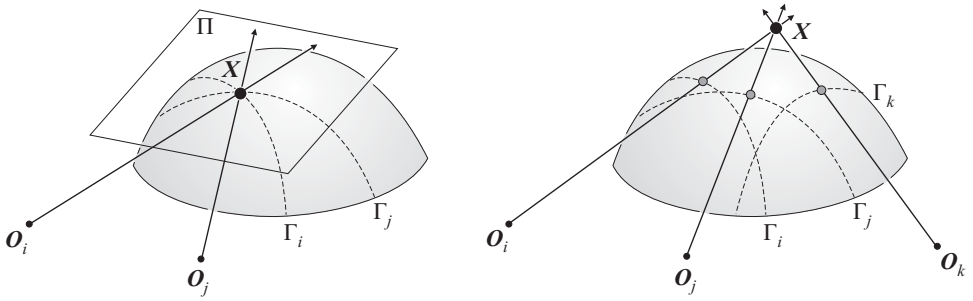

(a) Frontier point (b) Intersection point

Figure 3. Two types of visual hull vertices. (a) X is a frontier point: The visual rays connecting camera centers O_i and O_j to the surface point X lie in the tangent plane Π to the surface at this point. Note that X lies on the intersection of rims Γ_i and Γ_j. (b) X is an intersection point: The three visual rays emanating from O_i, O_j, and O_k graze the surface at three distinct points (indicated in gray) on the respective rims Γ_i, Γ_j and Γ_k, and then meet in space at X.

1-3) establishing oriented constraints used at various stages of the algorithm. To keep the presentation self-contained, we give abbreviated proofs of these results in Appendix D. Section 5 describes practical details of our implementation and Section 6 demonstrates results on several challenging real-world datasets and presents a comparison with another state-of-the-art visual hull construction algorithm (Franco and Boyer, 2003). Finally, Section 7 concludes with a summary of our contributions and a discussion of our target application of 3D photography.

2. Related Work

One major branch of visual hull study is theoretical, focusing on characterizing the shape that is consistent with the silhouettes of the target object observed from *every possible viewpoint*. Significantly, even in this case the visual hull cannot always exactly reproduce the object, since "dents" or concave parts of the surface will never appear on its silhouettes. There exist algorithms for computing the "limit" visual hull of polyhedral and smooth objects, in 2D and in 3D (Laurentini, 1994; Petitjean, 1998; Bottino and Laurentini, 2004) but they

assume that a 3D geometric model of the target object is available. In this article, we consider instead the more practical task of computing the visual hull of an unknown object observed from a finite number of known viewpoints.

Historically, the main strategy for computing the visual hull has been to directly implement the intersection of visual cones in 3D. The main advantage of volume intersection algorithms is that they (in principle) work with any combination of calibrated input viewpoints and make no assumptions about the object shape, e.g., smoothness or topology. The oldest such algorithm dates back to Baumgart's PhD thesis (1974), where a polyhedral visual hull is constructed by intersecting the viewing cones associated with polygonal approximations to the extracted silhouettes. A major disadvantage of such algorithms is that general 3D polyhedral intersections are relatively inefficient for the special-case problem of intersecting visual cones, and can suffer from numerical instabilities. An alternative technique for visual hull construction is to approximate visual cones by voxel volumes (Martin and Aggarwal, 1983; Potmesil, 1987; Ahuja and Veenstra, 1989; Srivastava and Ahuja, 1990; Szeliski, 1993). Voxel carving is not susceptible to numerical difficulties that can arise in exact computations with polyhedra. Moreover, its running time depends only on the number of input cameras and on the resolution of the volumetric representation, not on the intrinsic complexity of the visual hull. Parallel implementations of voxel carving can even achieve real-time performance for such applications as 3D action reconstruction (Matsuyama et al., 2004). On the other hand, volumetric visual hulls tend to suffer from quantization artifacts, and require an extra step, e.g., the *marching cubes algorithm* (Lorensen and Cline, 1987), to be converted to standard polygonal models. Moreover, voxel-based models do not retain any information about the intrinsic structure of the visual hull, i.e., locations of intersection curves and different cone strips — information that is required by our subsequent approach to high-fidelity high-resolution image-based modeling (Furukawa and Ponce, 2006).

Recent advances in image-based rendering and multi-view geometry have resulted in new efficient algorithms that avoid general 3D intersections by taking advantage of epipolar geometry. Matusik et. al. (2000) describe a fast, simple algorithm that involves image-based sampling along visual rays emanating from a virtual camera. The main limitation of this algorithm is that its output is view-dependent: If one wishes to render the visual hull from a new virtual viewpoint, one must re-run the construction algorithm. Another disadvantage is that image-based visual hulls require custom-built rendering routines. Subsequent work (Boyer and Franco, 2003; Franco and Boyer, 2003; Matusik et al., 2001; Shlyakhter et al., 2001) extends the idea behind image-based visual hulls to produce view-independent polyhedral models. The most important contribution of these newer algorithms is the reduction of 3D polyhedral intersections to 2D — a strategy that will also be followed in this article.

In practical applications, one is often interested in reconstructing an object from a video clip taken by a camera following a continuous trajectory. However, volume intersection techniques are ill-adapted to this task, which involves handling large numbers of almost coincident visual cones. In this case, assuming that the object is smooth, differential techniques of *shape from deforming contours* (Cipolla and Giblin, 2000) become more appropriate. The foundation for these techniques is given by mathematical relationships between the *contour generator* or *rim* where the visual cone is tangent to the object and its projection in the image plane, known as the *apparent contour* or *outline* (recall Figure 1). One of the most basic facts is that observing a smooth point on the apparent contour in the image is sufficient to reconstruct the tangent plane to the object in space. If the camera moves continuously, the rim gradually "slips" along the surface, and the surface may be reconstructed as the envelope of its tangent planes. This is volume intersection in an infinitesimal sense, and the shape obtained as a result of such an algorithm is also a visual hull. This approach

typically requires that the target objects be smooth, and precludes self-occlusion or changing topology of evolving contours.

Koenderink (1984) was the first to elucidate the relationship between the local geometry of the 3D surface and the geometry of the 2D contour in a single image. Giblin and Weiss (1987) have introduced a reconstruction algorithm for three-dimensional objects assuming orthographic projection and camera motion along a great circle. Subsequent approaches have generalized this framework to handle perspective projection and general (known) camera motions (Arbogast and Mohr, 1991; Cipolla and Blake, 1992; Vaillant and Faugeras, 1992; Boyer and Berger, 1997). All these approaches make extensive use of differential geometry, and focus on estimating local properties of the surface, such as depth and Gaussian curvature — computations that require approximating first- and second-order derivatives of image measurements and thus tend to be sensitive to noise and computation error. Our approach also assumes smooth surfaces and uses techniques of differential geometry to establish local properties of visual hulls. However, our reconstruction algorithm does not rely on approximations of local surface shape or curvature — the entity we compute is *exactly* the visual hull. In addition, unlike infinitesimal methods, ours does not make restrictive assumptions concerning self-occlusion or topology changes of the image contours.

The visual hull construction method presented in this article is based on ideas introduced in (Lazebnik et al., 2001; Lazebnik, 2002). These ideas have also served as a basis for an efficient algorithm to compute an exact polyhedral visual hull (Franco and Boyer, 2003), and a hybrid algorithm combining voxel carving and surface-based computation (Boyer and Franco, 2003). Other recent developments include visual hull construction from uncalibrated images (Sinha and Pollefeys, 2004), as well as Bayesian (Grauman et al., 2003; Grauman et al., 2004) and algebraic dual-space approaches to visual hull reconstruction (Brand et al., 2004). To our knowledge, our method remains the only one that computes

an exact image-based combinatorial representation of the visual hull while relying solely on oriented projective constraints.

3. Mathematical Preliminaries

Before we start the discussion of our visual hull construction algorithm in Section 4, let us briefly introduce the mathematical machinery used in the rest of our presentation. This machinery consists of basics of oriented projective geometry (Section 3.1) and oriented representations of cameras and apparent contours (Section 3.2).

3.1. Oriented Projective Geometry

In this presentation, we model the 2D camera plane and the ambient 3D space, as *oriented projective spaces* $\mathbb{T}^2$ and $\mathbb{T}^3$, respectively. By analogy with the standard projective spaces $\mathbb{P}^2$ and $\mathbb{P}^3$, which are formed by identifying all vectors of $\mathbb{R}^3$ and $\mathbb{R}^4$ that are *nonzero* multiples of each other, $\mathbb{T}^2$ and $\mathbb{T}^3$ are formed by identifying all vectors of $\mathbb{R}^3$ and $\mathbb{R}^4$ that are *positive* multiples of each other (Stolfi, 1991). Note that according to its definition, the *oriented plane* $\mathbb{T}^2$ is topologically equivalent to a 2-sphere, so in effect, we will be dealing with omnidirectional cameras. Uppercase letters will denote *flats* (points, lines, and planes) in $\mathbb{T}^3$, and lowercase letters will denote flats in $\mathbb{T}^2$. In the sequel, we will assume fixed (but arbitrary) coordinate systems for all spaces of interest, and identify all flats with their homogeneous coordinate vectors, which in the oriented setting are unique up to a positive scale factor.

A line is spanned by two distinct points, i.e., a *proper 2-simplex*, and a plane is spanned by three non-collinear points, i.e., a *proper 3-simplex*. Two simplices spanning the same flat are said to have the same orientation when they are related by an *orientation-preserving* transformation represented by a matrix with a positive determinant. All the simplices of a given flat form two classes under

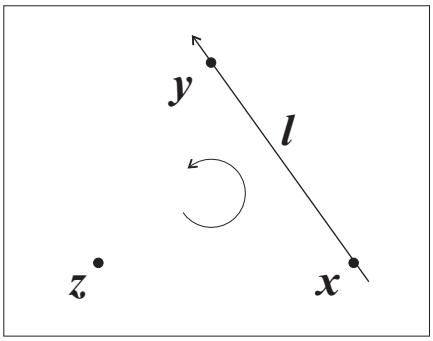

$$l \vee z = x \vee y \vee z = |x, y, z| > 0$$

Figure 4. Relative orientation of a line and a point in 2D. The counterclockwise arrow indicates the positive orientation of the 2D universe.

this equivalence relation, and an *oriented* flat is a flat to which an orientation has been assigned by choosing one of these two classes as "positive." To obtain the simplex spanning the *join* of two flats, we simply concatenate the simplices that span the two respective flats *in that order*. For example, in Figure 4 the join of two points x and y is the oriented line l. This operation is denoted as $l = x \vee y$, and the homogeneous coordinate vector of l is given by the cross-product $x \times y$. The join of three points x, y, and z spans either the *positive* or the *negative* universe of $\mathbb{T}^2$. The homogeneous (Plücker) coordinate of the universe is a scalar, and it is given by the 3×3 determinant $|x, y, z|$. Assuming that right-handed triangles in $\mathbb{T}^2$ have been chosen as the positive ones, a necessary and sufficient condition for x, y, and z to span the positive universe is $|x, y, z| > 0$ (when $|x, y, z| = 0$ then the three points are collinear, and do not span the universe at all). Equivalently, we can express the universe as the join of the line $l = x \vee y$ and the point z. The sign of $l \vee z = l^T z$ determines the *relative orientation* of l and z. Whenever $l \vee z > 0$ (resp. $l \vee z < 0$), we will say that z lies on the positive (resp. negative) side of l.

3.2. Cameras and Contours

Let us suppose that we are observing some solid Ω using n perspective cameras.[1] The solid is bounded by a smooth surface whose shape is to be inferred based on the silhouette boundaries or *outlines* $\gamma_1, \ldots, \gamma_n$ observed in the image planes of the cameras. Let us assume that each outline possesses a *regular parametrization* $u \mapsto x(u) = \Big(x_1(u), x_2(u), x_3(u)\Big)^T$ such that the *derivative point*[2] $x'(u) = \Big(x_1'(u), x_2'(u), x_3'(u)\Big)^T$ is not identically zero nor a scalar multiple of $x(u)$. This condition ensures that the *tangent line* $t(u)$, formed by the join $x(u) \vee x'(u)$ of the outline point $x(u)$ and its derivative point $x'(u)$, is everywhere well defined.[3] We assume that the outline is naturally oriented in the direction of increasing parameter values, and require this orientation to be such that the image of the interior of Ω is always located on the positive (left) side of the outline (refer back to Figure 1 for an illustration of this convention). Provided that this orientation convention is met, the silhouettes are allowed to have holes and multiple connected components.

In addition to the outlines, our algorithm requires as input an estimate of the epipolar geometry of the scene, consisting of *fundamental matrices* $\mathcal{F}_{ij}$ and *epipoles* e_{ij} between each pair of cameras. The issue of finding properly oriented fundamental matrices and epipoles has been addressed in several publications (Werner and Pajdla, 2001a; Werner and Pajdla, 2001b; Chum et al., 2003). In practice, however, one usually does not compute the epipolar geometry between each pair of cameras from scratch. Instead, it is more convenient to compute the fundamental matrices based on properly oriented projective esti-

[1] For the sake of our implementation, we assume that the object is inside the viewing volume of each camera. Unlike some voxel-based methods, we do not deal with the issue of partial observation.

[2] In homogeneous coordinates, the successive derivatives $x^{(i)}(u)$ represent points in $\mathbb{T}^2$ (by contrast, when a non-homogeneous coordinate representation is used, as in the Euclidean case, derivatives are thought of as vectors instead of points).

[3] Note that the smoothness assumption is violated at a small number of isolated contour locations corresponding to T-junctions. However, in the implementation we ignore T-junctions and assume that the contour is everywhere smooth. This introduces only a small amount of approximation error to the "true" silhouettes, and does not affect the procedure for visual hull computation, since the visual hull is well defined as the intersection of the visual cones formed by back-projecting the objects' silhouettes regardless of whether the contours bounding the silhouettes are non-smooth or contain T-junctions.

mates of the camera matrices $\mathcal{P}_1, \ldots, \mathcal{P}_n$. To be more specific, to ensure proper orientations of the camera projection matrices, we must enforce the constraint that any point x_i observed in the image plane of the ith camera is equal up to a *positive* scale factor to the computed projection $\mathcal{P}_i X$, denoted $x_i \simeq \mathcal{P}_i X$. These sign consistency constraints can either be built into the projective bundle adjustment procedure or imposed a posteriori using the simple "sign flipping" technique described in Hartley (1998).[4] Assuming that all camera matrices have thus been assigned consistent orientations, fundamental matrices and epipoles can be computed using the properly oriented formulas given in Appendix A.

4. Computing the Visual Hull

This section develops our method for computing the visual hull using only oriented projective constraints. A high-level summary of the proposed algorithm is given in Figure 5. The visual hull is constructed in two stages: First, we find the *1-skeleton*, i.e., the set of all vertices and edges of the visual hull; and second, we "fill in" the interiors of the cone strips.

The first stage is implemented as an incremental algorithm that, at the end of the ith iteration, produces the complete 1-skeleton of the intersection of visual cones numbered 1 through i. To add the $(i+1)$st visual cone, the existing 1-skeleton is modified in two steps: First, all parts of the existing 1-skeleton that fall outside the new cone (and thus cannot belong to the visual hull by definition) are clipped away; and second, intersection curves of the $(i+1)$st cone with all previous cones are traced and clipped against all pre-existing views. After processing all n cones in this fashion, we have a complete combinatorial representation of the boundaries of all n cone strips composing the visual hull surface, but we do not yet have an explicit representation of the strips themselves.

[4] Since we restrict ourselves to the oriented projective setting where the cameras are in effect spherical, we do not have to deal with the more troublesome cheirality or visibility constraints that arise when computing Euclidean upgrades. See Nistér (2004) for a recent treatment of this issue.

To obtain such a representation, we triangulate the strips using a sweepline algorithm.

Note that our incremental algorithm is not "optimal" from the viewpoint of computational efficiency, since the results of many of its intermediate computations do not contribute to the final visual hull. However, it has the advantage of being very simple, and, as shown in Section 6.3, can outperform a non-incremental algorithm. It must also be noted that an incremental strategy can be preferable in certain practical situations. For example, it can be used with an experimental setup in which input images are acquired sequentially. Instead of waiting until all images of the object have been taken, it may be preferable to build an intermediate model based on the available data. Moreover, in such a system, the user could halt the computation as soon as the model achieves an acceptable degree of approximation to the target object.

The next three sections will describe the details of the algorithm's three key subroutines: tracing intersection curves between pairs of visual cones (Section 4.1); clipping interesection curves (Section 4.2); and triangulating the cone strips (Section 4.3).

4.1. Tracing an Intersection Curve

Let us consider the cones associated with cameras i and j, whose surfaces are formed by back-projecting the outlines γ_i and γ_j, parametrized by u and v, respectively. Their intersection curve, denoted I_{ij}, consists of 3D points X for which there exists a choice of parameters u and v such that the rays formed by back-projecting the outline points $x_i(u)$ and $x_j(v)$ intersect. This is expressed by the well-known *epipolar constraint*

$$f(u, v) = x_j(v)^T \mathcal{F}_{ij} x_i(u) = 0\,, \tag{1}$$

where $\mathcal{F}_{ij}$ is the fundamental matrix between views i and j. Note that (1) can be seen as an implicit equation of a curve δ_{ij} in the joint parameter space of γ_i

Input: Outlines $\gamma_1, \ldots, \gamma_n$, fundamental matrices $\mathcal{F}_{ij}$.
Output: A combinatorial representation of the visual hull boundary.

[Find the 1-skeleton.]
For $i = 2, \ldots, n$
  Clip each existing edge of the 1-skeleton against γ_i.
  For $j = 1, \ldots, i-1$
    Trace the intersection curve I_{ij}.
    For $k = 1, \ldots, i-1$, $k \neq j$
      Clip each edge of I_{ij} against γ_k.
    End For
  End For
End For

[Find the visual hull faces.]
For $i = 1, \ldots, n$
  Triangulate the ith cone strip.
End For

Figure 5. Overview of the visual hull construction algorithm.

and γ_j.[5] Thus, instead of directly tracing the intersection curve I_{ij} in 3D, we can trace δ_{ij} in the (u, v)-space. This strategy has been inspired by an algorithm for finding the intersection of two ruled surfaces published in the computer-aided design community (Heo et al., 1999).

Note. In the oriented setting, the epipolar constraint $f(u, v) = 0$ is actually not a sufficient condition for the corresponding visual rays to intersect in space. That is, given two points $x_i(u)$ and $x_j(v)$ that satisfy (1), there does not always exist a physical 3D point X such that $x_i(u) \simeq \mathcal{P}_i X$ and $x_j(v) \simeq \mathcal{P}_j X$. Appendix B (Proposition 4) gives the additional *epipolar consistency* condition needed to guarantee the existence of X, and describes a simple way to eliminate the connected components of δ_{ij} that do not meet this condition. In our subsequent presentation, we will use δ_{ij} to denote only the set of *consistent* components of the curve implicitly defined by $f(u, v) = 0$.

[5] Since we allow silhouettes to have holes and multiple connected components, the outlines consist of one or more disjoint simple loops, and the parameter space has the topology of a collection of one or more tori.

4.1.1. *Critical Points of an Intersection Curve*

Our general strategy for tracing δ_{ij} is as follows: We break up the implicitly defined curve into *branches* where one variable (say, v) can be expressed as a function of the other (u) and then trace each branch separately, recording along the way the global information about connectivity of the branches. This subsection will treat the first step towards implementing this strategy, namely, specifying the *critical points* along which the curve is to be broken up, and characterizing the local behavior of δ_{ij} in the neighborhood of each of these points.

Let f_u and f_v denote partial derivatives of f with respect to u and v. Then the derivative of v with respect to u, given by $\frac{\mathrm{d}v}{\mathrm{d}u} = -\frac{f_u}{f_v}$, is undefined wherever $f_v = 0$. At any such point, v cannot be locally expressed as a function of u. Thus, we define points where $f_v = 0$ as critical. To preserve symmetry between the variables u and v, we also expand the definition to points where $f_u = 0$. Then all critical points (u_0, v_0) of of δ_{ij} can be classified into the following three types:

1. $f_u(u_0, v_0) = 0, \quad f_v(u_0, v_0) = 0;$
2. $f_u(u_0, v_0) = 0, \quad f_v(u_0, v_0) \neq 0;$
3. $f_u(u_0, v_0) \neq 0, \quad f_v(u_0, v_0) = 0.$

To understand the geometric significance of these types, let us begin by computing the derivatives f_u and f_v:

$$f_u = x_j^T \mathcal{F}_{ij} x_i' = x_i'^T \mathcal{F}_{ji} x_j = x_i' \vee l_{ij} = |x_i, x_i', e_{ij}|\,, \tag{2}$$

$$f_v = x_j'^T \mathcal{F}_{ij} x_i = x_j' \vee l_{ji} = |x_j, x_j', e_{ji}|\,. \tag{3}$$

When $f_u = 0$, x_i is distinguished by the geometric property that its tangent line $t_i = x_i \vee x_i'$ passes through the epipole e_{ij}, or equivalently, that the derivative point x_i' lies on the *epipolar line* $l_{ij} = e_{ij} \vee x_i$ (Figure 6). When $f_v = 0$, the point x_j in the jth view is analogously characterized by epipolar tangency. Of particular

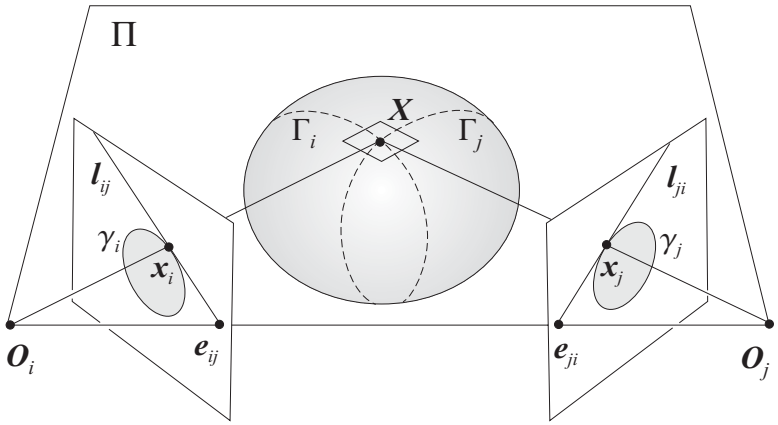

Figure 6. Frontier point (see text).

interest is the case of simultaneous epipolar tangency, when $f_u = 0$ and $f_v = 0$. Then x_i and x_j are projections of a *frontier point* X that is the intersection of the rims Γ_i and Γ_j on the surface (Rieger, 1986; Porrill and Pollard, 1991; Cipolla et al., 1995). The surface tangent plane at X coincides with the (unoriented) *epipolar plane* defined by O_i, O_j and X. The epipolar plane also coincides with the tangent planes of the ith and jth visual cones at X, and the direction of the intersection curve, which is normally given by the line of intersection of the cones' tangent planes, is locally undefined. Therefore, a frontier point gives rise to a singularity of the intersection curve.

In accordance with the above analysis, if a critical point (u_0, v_0) is of type 1, then $x_i(u_0)$ and $x_j(v_0)$ are images of a frontier point visible in both views (Figure 7, top); if it is of type 2, $x_i(u_0)$ is an epipolar tangency in the ith view and $x_j(v_0)$ is a transversal intersection of the epipolar line $l_{ji} = \mathcal{F}_{ij}x_i(u_0)$ with the outline γ_j (Figure 7, middle); and if it is of type 3, $x_j(v_0)$ is an epipolar tangency in the jth view and $x_i(u_0)$ is a transversal intersection of $l_{ij} = \mathcal{F}_{ji}x_j(v_0)$ with γ_i (Figure 7, bottom). In the joint parameter space, critical points of type 1 correspond to singularities of δ_{ij}, while critical points of types 2 and 3 correspond to local extrema in v- and u-directions, respectively. Using second-order techniques for analyzing singularities of an intersection curve of two implicit surfaces (Hoff-

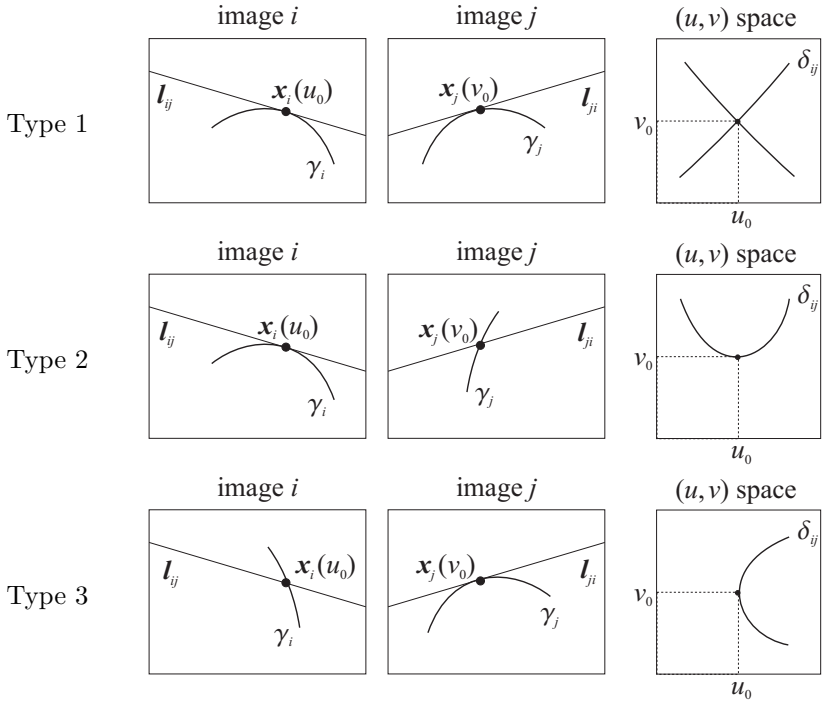

Figure 7. Critical point types (see text).

mann, 1989; Owen and Rockwood, 1987), it is straightforward to determine the geometry of δ_{ij} in the neighborhood of a singularity:

Proposition 1. *Let (u_0, v_0) be a point on δ_{ij} such that $f_u(u_0, v_0) = 0$ and $f_v(u_0, v_0) = 0$. Then δ_{ij} in the neighborhood of (u_0, v_0) has an X-shaped crossing, that is, it consists of two transversally intersecting curve branches with tangent vectors given by $(a, 1)$ and $(-a, 1)$, where $a = \sqrt{-\frac{f_{vv}}{f_{uu}}}$.*

The proof of the above proposition is given in Appendix D.1. Note that instead of thinking of a singularity as an X-shaped crossing, we can think of it as a vertex with four incident branches. The tangent vectors pointing along each of these branches are $(a, 1)$, $(-a, 1)$, $(a, -1)$ and $(-a, -1)$. Each of these vectors points into a different "quadrant" obtained by partitioning a neighborhood of (u_0, v_0) with the lines $u = u_0$ and $v = v_0$. Consequently, we can uniquely identify each of the four branches by the *sign label* of the quadrant it locally occupies, i.e., $++$, $+-$, $-+$, $--$ (Figure 8, left). In order to assign analogous sign labels to

branches incident on critical points of type 2 and 3, we first have to determine whether these critical points are local maxima or minima in the direction of u and v, respectively. The next proposition, which is proved in Appendix D.2, tells us how to make this determination, resulting in the complete classification of critical point types shown in Figure 8.

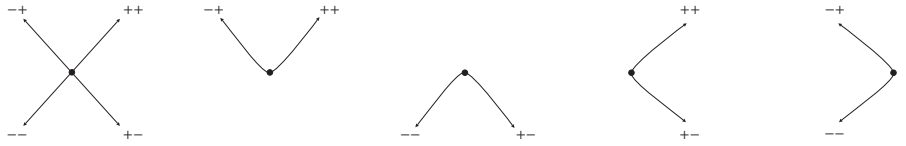

Type 1	Type 2A	Type 2B	Type 3A	Type 3B
$f_u = 0,\ f_v = 0$	$f_u = 0,\ f_v \neq 0$	$f_u = 0,\ f_v \neq 0$	$f_u \neq 0,\ f_v = 0$	$f_u \neq 0,\ f_v = 0$
	local min	local max	local min	local max

Figure 8. A complete classification of critical points with sign labels of incident branches. The figure shows sign labels for the branches incident on each critical point. The first (resp. second) sign identifies whether the value of u (resp. v) increases or decreases as we follow a particular branch away from (u_0, v_0) (note that by construction, a branch of the curve must be monotone, i.e., uniformly nondecreasing or nonincreasing, with respect to both the u- and the v-axis).

Proposition 2. *Consider the points $x_i = x_i(u_0)$ and $x_j = x_j(v_0)$ on γ_i and γ_j such that that (u_0, v_0) is a type 2 critical point of δ_{ij}. Consider the derivatives*

$$\begin{aligned} f_v &\simeq |x_j, x_j', e_{ji}| \simeq t_j \vee e_{ji} \quad \textit{and} \\ f_{uu} &= x_i'' \vee l_{ij} \simeq \begin{cases} |x_i, x_i', x_i''|\,, & \textit{if } t_i \simeq l_{ij} \\ -|x_i, x_i', x_i''|\,, & \textit{if } t_i \simeq -l_{ij}\,. \end{cases} \end{aligned} \tag{4}$$

Then (u_0, v_0) is a local maximum (resp. minimum) in the v-direction if the signs of f_v and f_{uu} are the same (resp. opposite).

Analogously, if (u_0, v_0) is a type 3 critical point of δ_{ij}, then it is a local maximum (resp. minimum) in the u-direction if the signs of f_u and f_{vv} are the same (resp. opposite).

Let us consider the geometric meaning of the sign of f_{uu}. Based on Eq. (4), we can see that this sign depends on two factors: first, whether the epipolar line l_{ij} coincides with the tangent line t_i to γ_i at x_i or whether the two lines have opposite orientations; and second, whether the quantity $\kappa_i = |x_i, x_i', x_i''|$ is

positive or negative. Significantly, κ_i is an *oriented projective invariant* that tells us about the local shape of γ_i at x_i: if κ_i is positive (resp. negative), then γ_i is *convex* (resp. *concave*) in the neighborhood of x_i (Lazebnik and Ponce, 2005). Thus, we can see that the characterization of critical point types, which is a crucial prerequisite for the intersection curve tracing algorithm presented in the next section, depends on elementary local geometric properties of contours, their tangents, and epipolar lines.

We can obtain an alternative interpretation of f_{uu} by thinking of the task of searching for all frontier points in the ith view as finding the zeros of $f_u = t_i \vee e_{ij}$. Since the geometric interpretation of the sign of f_u is the relative orientation of the tangent line t_i and the epipole e_{ij}, and since f_{uu} is the first derivative of this function, the sign of f_{uu} at a point when $f_u = 0$ tells us whether this relative orientation is changing from negative to positive or vice versa. When $f_{uu} > 0$, the tangent line is turning in such a way that the epipole begins to appear on its positive side; the situation is reversed for $f_{uu} < 0$. We will make use of this interpretation in Section 5.1 when defining frontier point classifications for discretely sampled contours.

4.1.2. *The Tracing Algorithm*

Given the characterization of critical points derived in the previous section, it is now straightforward to develop an algorithm for tracing δ_{ij}. The algorithm begins by finding all critical points of the intersection curve and determining their types using the test of Proposition 2. Each critical point, depending on its type, serves as the origin of at most two branches leading in the increasing direction of u, i.e., having sign labels $++$ or $+-$. As can be seen from Figure 8, critical points of types 1 and 3A have both $++$ and $+-$ branches, those of type 2A have one $++$ branch, those of type 2B have one $+-$ branch, and those of type 3B have none. Accordingly, the algorithm uniquely identifies each branch of the intersection curve by noting its origin and sign label ($++$ or $+-$), and proceeds to trace the branch away from its origin, stopping when the second

endpoint is detected. The steps of finding critical points and tracing individual branches are explained in more detail below.

Critical points are found as follows: For each epipolar tangency in the ith view, i.e., a contour point $x_i(u)$ such that $|x_i, x_i', e_{ij}| = 0$, we draw the corresponding epipolar line $l_{ji} = F_{ij}\, x_i$ in the jth view and find all intersections of this line with γ_j. For each point of intersection $x_j(v)$, we add the pair of parameter values (u, v) to the list of critical points. In this way, all the critical points of type 2 are identified. To find all critical points of type 3, we carry out the same procedure with the roles of the ith and jth views interchanged. Extra care is required to correctly identify critical points of type 1 that occur whenever $x_i(u)$ and $x_j(v)$ are epipolar tangencies lying along exactly matching epipolar lines. However, in practice this situation never occurs: Because of (unavoidable) errors in contour extraction and/or camera calibration, whenever we have an epipolar tangency in one image, the corresponding epipolar line in the other image either misses the contour entirely, or intersects it in a pair of nearby points. Thus, instead of a singularity or a critical point of type 1, we observe a pair of critical points of type 2 or 3 (Figure 9). This also affects the local topology of the visual hull surface: instead of two cone strips that cross each other at the singularity, as in the ideal case depicted in Figure 2, one strip becomes interrupted or "covered" by the other one.

Each intersection curve branch is traced as follows: At each step, a fixed increment is added to the current value of u, and the corresponding value of v is found by locally searching along γ_j for the nearest intersection with the epipolar line $l_{ji}(u) = \mathcal{F}_{ij} x_i(u)$. More precisely, let (u_{t-1}, v_{t-1}) be the point of the branch found in the previous iteration of the tracing procedure, and let u_t be the next value of u. Then the corresponding v_t is the parameter value of the outline point nearest to $x_j(v_{t-1})$ where $l_{ji}(u_t)$ intersects γ_j (Figure 10, left). Note that we search for v_t in the increasing (resp. decreasing) direction of v if the sign label of the current branch is $++$ (resp. $+-$). The trace terminates when either γ_i or

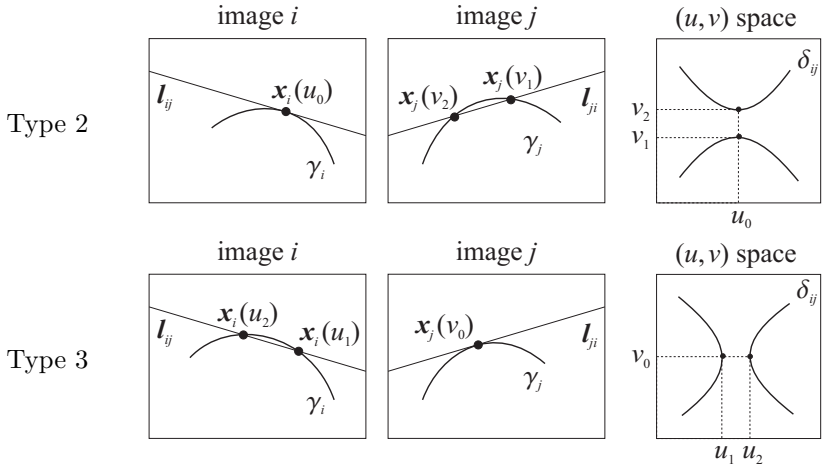

Figure 9. Top: The contour γ_j has been "perturbed" so that the epipolar line l_{ji} intersects γ_j in two points $x_j(v_1)$ and $x_j(v_2)$. As a result, δ_{ij} loses the crossing and acquires two critical points of type 2. Bottom: An analogous perturbation of γ_i results in a pair of type 3 critical points.

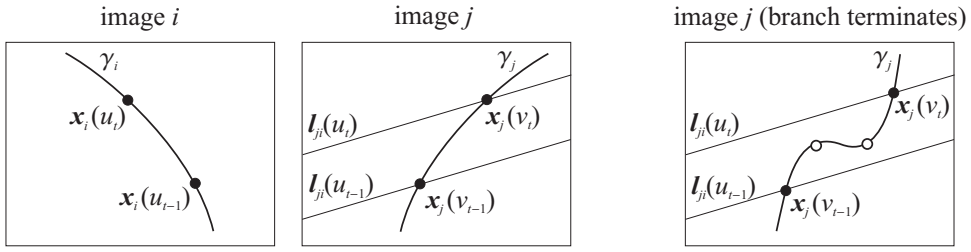

Figure 10. The incremental process for tracing an intersection curve (see text). The white points on the right part of the figure show two epipolar tangencies of γ_j in the interval $[v_{t-1}, v_t]$, indicating that the trace of the current branch needs to terminate.

γ_j contains epipolar tangencies in the interval $[u_{t-1}, u_t]$ or $[v_{t-1}, v_t]$ (Figure 10, right) and the critical point first encountered is recorded as the second vertex of the current branch. For completeness, we must also consider the situation when the intersection curve has no critical points at all. This can happen, for example, when the target object is convex and the line connecting the camera centers O_i and O_j passes through its interior, so that the epipoles fall inside the silhouettes in both views and neither outline has epipolar tangencies. In such a case, we simply pick an arbitrary starting point u_0 to begin the tracing and continue until the current value of u reaches u_0 again.

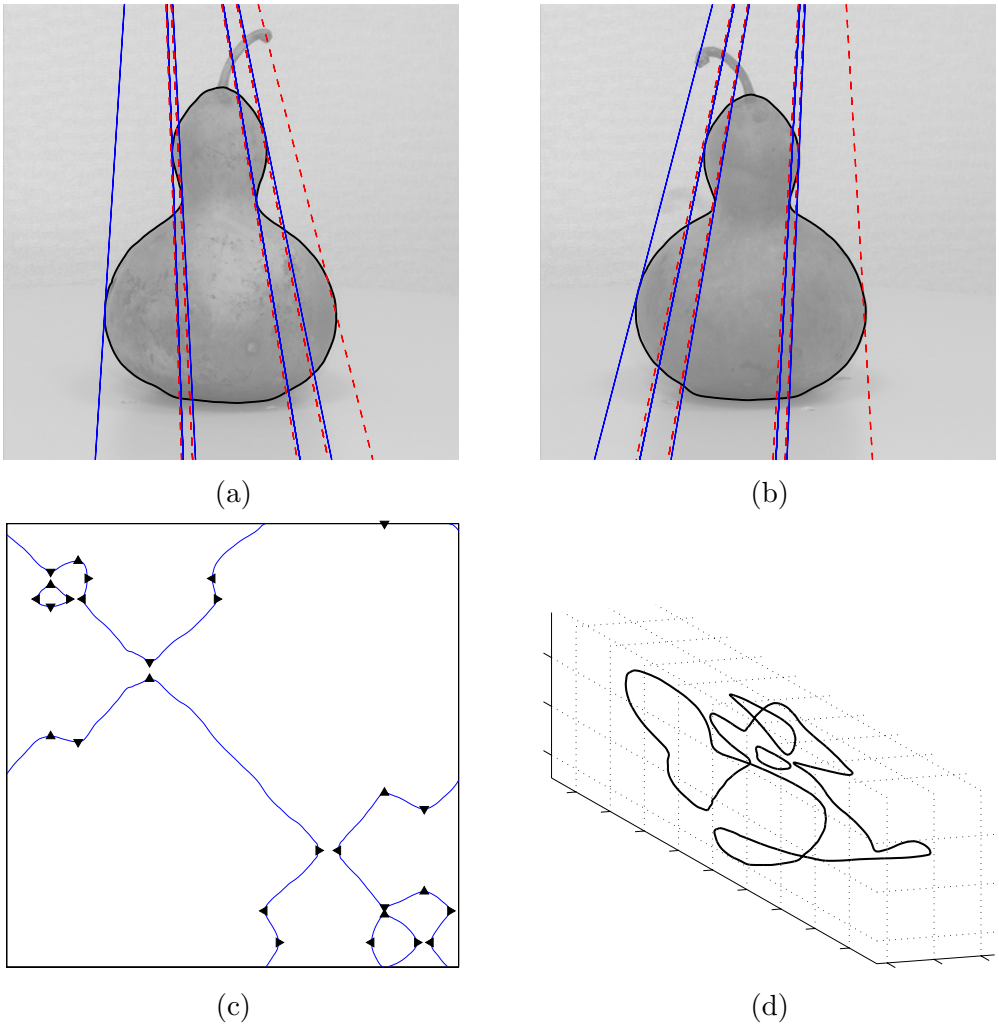

Figure 11. (a), (b) Two views with outlines and epipolar lines corresponding to critical points. The epipolar lines tangent to the outlines are solid, and the epipolar lines corresponding to frontier points in the other view are dashed. Note that (a) and (b) show the gourd from opposite sides, so that the leftmost epipolar line in (a) corresponds to the rightmost epipolar line in (b) and so on. (c) The intersection curve δ_{ij}. The horizontal axis is u and the vertical axis is v. Critical points of types 2A, 2B, 3A, and 3B are indicated by ▼, ▲, ◄, and ►, respectively. (d) The intersection curve in 3D.

Figure 11 illustrates the output of the intersection curve tracing algorithm using an example of two views of a gourd. As part (d) of the figure shows, we can easily obtain a 3D representation of I_{ij} (in a projective coordinate system, of course) by triangulating the pairs of contour points $x_i(u)$ and $x_j(v)$ corresponding to each (u, v) in δ_{ij}. A particularly simple linear triangulation method (Forsyth and Ponce, 2002) is as follows. Let X be the (unknown) coordinate vector of a

point on I_{ij}, and let $x_i(u) \simeq \mathcal{P}_i X$ and $x_j(v) \simeq \mathcal{P}_j X$ be its projections on the ith and jth contours. Then we can write the projection constraints as

$$\begin{cases} x_i \times \mathcal{P}_i X &= 0\,, \\ x_j \times \mathcal{P}_j X &= 0\,. \end{cases}$$

This is a system of six linear homogeneous equations in four unknowns whose least-squares solution gives us an estimate of X (note that there is a sign ambiguity in this estimate; it can be resolved by enforcing the orientation consistency of the original projection constraints).

4.2. Finding the 1-skeleton

Next, we move on to the second step of computing the visual hull: finding its *1-skeleton*, or the subset of its boundary comprised of segments of intersection curves between pairs of input views. When the visual hull is formed by intersecting only two cones, the 1-skeleton is simply the intersection curve between the two cones. With more than two cameras present in the scene, the task of computing the 1-skeleton becomes more complicated: We must determine which fragments of the $\binom{n}{2}$ different intersection curves actually belong to the visual hull, and then establish the connectivity of these fragments.

First, let us discuss how to compute the contribution of a given intersection curve I_{ij} to the 1-skeleton. Recall that the visual hull consists of points whose images do not fall outside the silhouette of the object in any input view. We enforce this property by projecting I_{ij} into each available view $k \neq i, j$ and "clipping away" the parts that fall outside the silhouette in the kth view. Let ι_{ij}^k denote the projection of I_{ij} into the kth view. This projection can be obtained either from a 3D representation of I_{ij}, or directly from δ_{ij} via an image-based *transfer* operation (see Appendix C for a brief treatment of oriented epipolar transfer). Following reprojection, we compute the subset of the curve ι_{ij}^k that also lies inside the kth silhouette (Figure 12). This operation involves "cutting" ι_{ij}^k along points where it intersects γ_k. As will be explained in Section 5.2, these points can be found efficiently with the help of a few simple data structures.

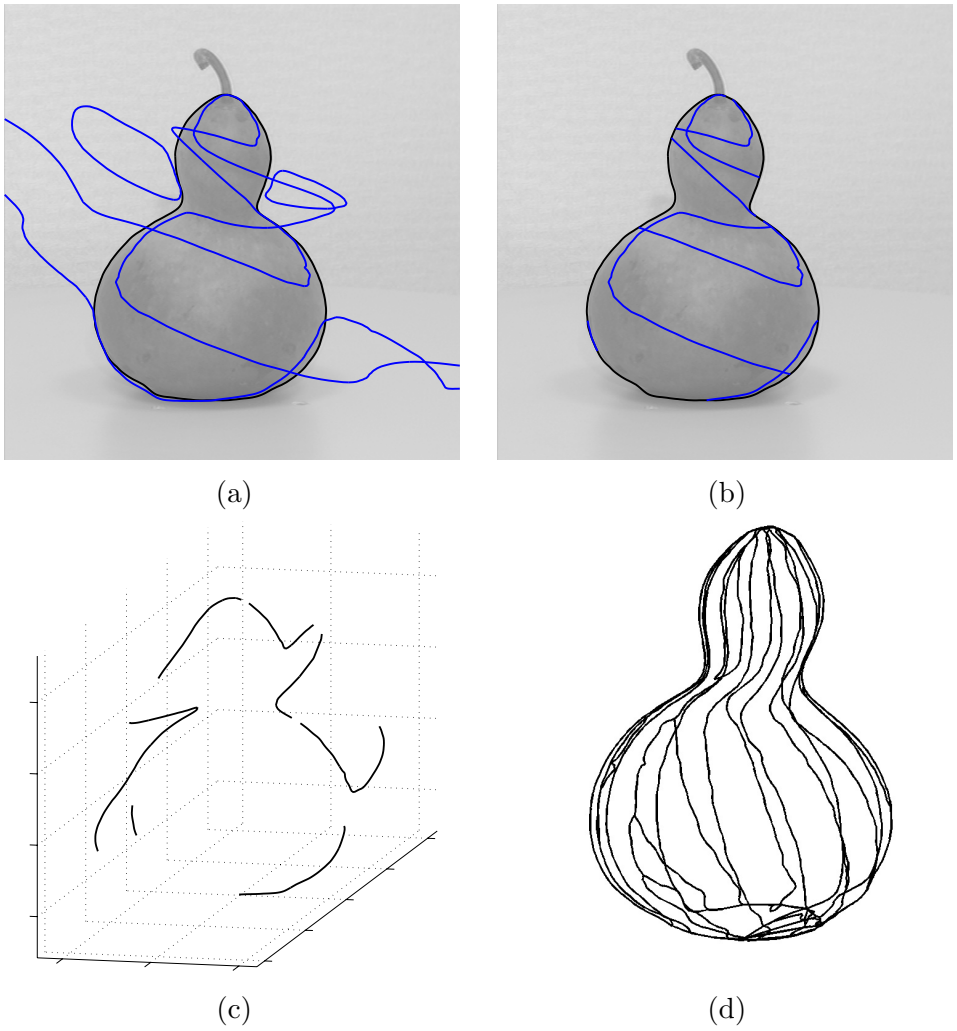

Figure 12. Clipping the intersection curve of Figure 11 against a third view of the gourd. (a) The reprojected intersection curve superimposed upon the third image. (b) The intersection curve clipped against the silhouette. (c) The clipped curve in 3D. (d) The complete 1-skeleton for nine views.

Consider a point x_k that simultaneously lies on γ_k and on ι_{ij}^k. It is easy to see (Figure 13) that x_k is the projection of an *intersection point* X in 3D that simultaneously belongs to the ith, jth, and kth visual cones. X can also be described as a trinocular stereo match of points on the three respective outlines, though in a generic situation, it is not a true physical point on the surface of the object being reconstructed.[6] Since X is the point of incidence of three segments

[6] For the intersection point to lie on the surface, the trifocal plane would have to be tangent to the object, which does not happen when the cameras are in general position.

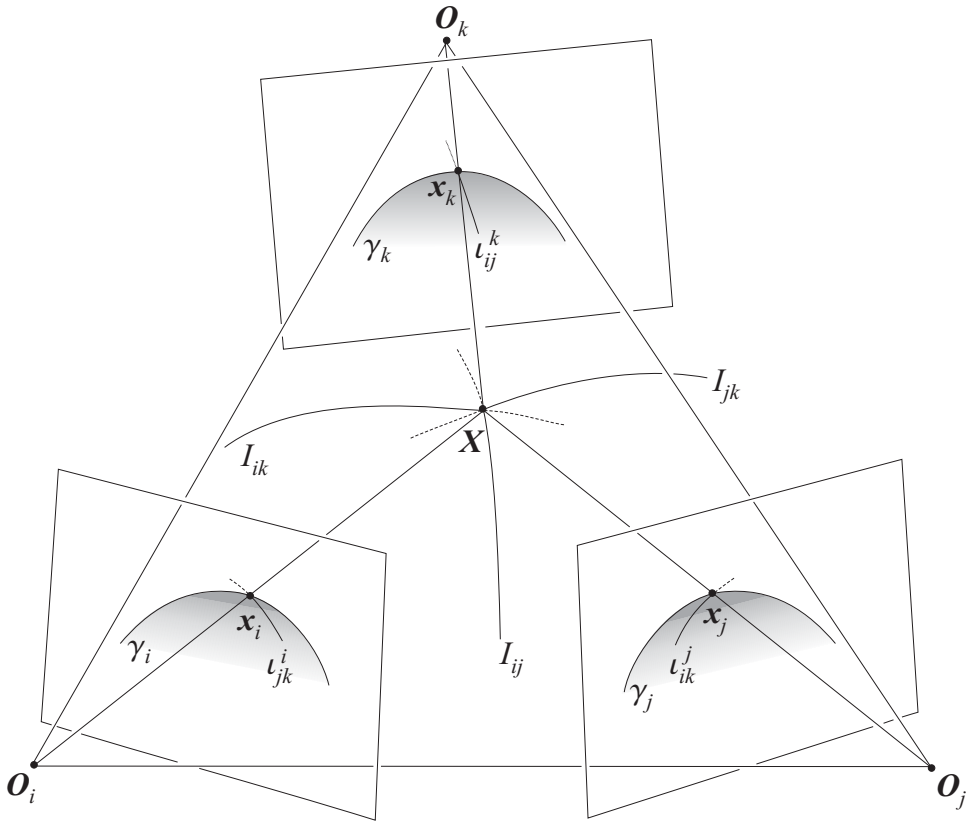

Figure 13. X is an intersection point between views i, j, and k. The thick black curves incident on X are fragments of I_{jk}, I_{ik}, and I_{ij} that belong to the 1-skeleton of the visual hull. The parts of the respective intersection curves that are "clipped away" by the ith, jth, and kth cones are dashed. The object Ω is not shown to avoid clutter.

belonging to the pairwise intersection curves I_{ij}, I_{jk}, and I_{ik}, it is found three times in the course of our procedure for computing the 1-skeleton: when clipping I_{jk} against the ith silhouette, when clipping I_{ik} against the jth silhouette, and when clipping I_{ij} against the kth silhouette. Therefore, after carrying out all the clipping operations, we must complete the combinatorial description of the 1-skeleton by joining the triple occurrences of each intersection point and recording the incidence of the corresponding intersection curve segments. Our implementation of the joining procedure will be discussed in Section 5.3.

The complete boundary of the visual hull consists of *strips* lying on the surfaces of the original visual cones (Figure 14). The 1-skeleton obtained at the end of the clipping stage gives us a complete combinatorial representation of all the strip boundaries, consisting of vertices that are critical points and intersection points, and edges that are segments of intersection curves. However, we do not yet have an explicit description of the strip interiors. To obtain such a description in the form of meshes suitable for rendering and visualization, we must *triangulate* the cone strips. Our triangulation algorithm is given in Figure 15. In the rest of this section, we give a high-level explanation of this algorithm, and in Section 4.3.1, we fill in the technical details necessary to its implementation, namely, the definitions of *linear ordering* and *front/back status* of strip edges.

The ith cone strip may be thought of as a collection of intervals along the continuous family of visual rays $L_i(u)$, each of which is formed by back-projecting the corresponding point $x_i(u)$ on γ_i. Accordingly, we perform triangulation by sweeping the visual ray $L_i(u)$ along the strip in the increasing direction of the contour parameter u. We can think of this operation as a 2D vertical line sweep standard in computational geometry if we imagine "cutting" the cone strip along

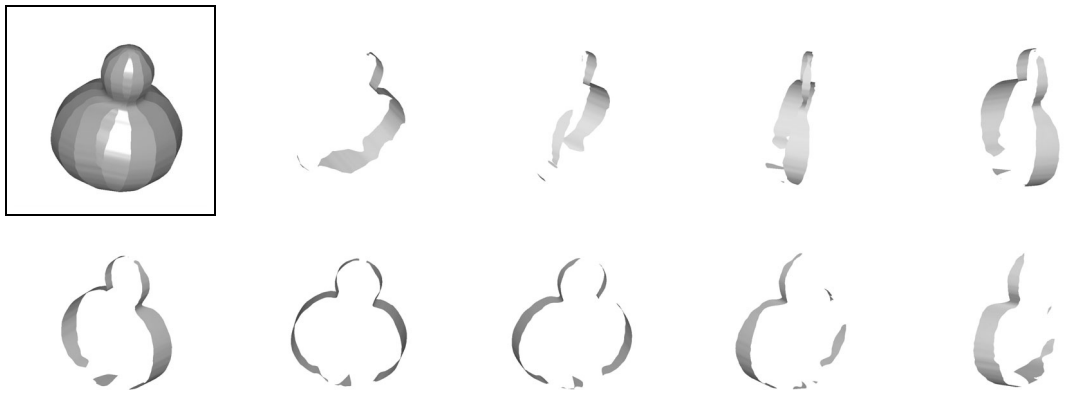

Figure 14. The visual hull of the gourd computed from nine views (top left) and the nine constituent cone strips.

Input: Cone strip.
Output: A triangulation of the cone strip.

Create event list by sorting the parameter values of the endpoints of all edges on the boundary of the cone strip. Initialize the active list with all edges that contain some starting position u_0.

For each event u_t
  [Fill in triangles from u_{t-1} to u_t.]
  For each pair (E, E') of adjacent edges in the active list such that
  E is a front edge and E' is a back edge
    Fill in triangles between E and E' in the interval $[u_{t-1}, u_t]$.
  End For
  [Update the active edge list.]
  If u_t is an event where an edge starts
    Insert edge into active list.
  Else If u_t is an event where an edge ends
    Delete edge from the active list.
  End If
End For

Figure 15. Overview of the cone strip triangulation algorithm.

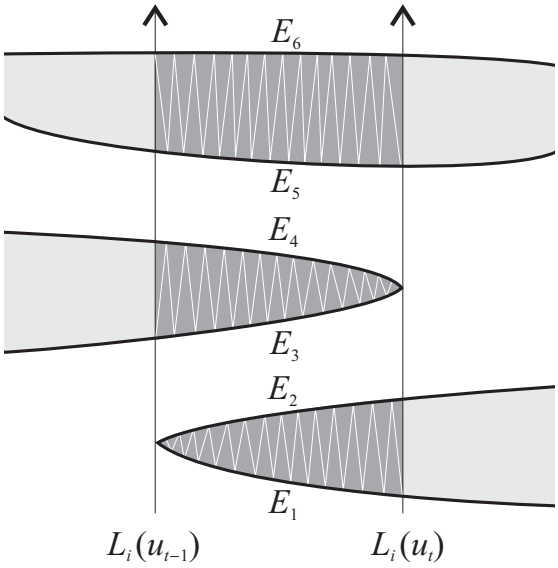

Figure 16. Triangulating a cone strip between two consecutive events u_{t-1} and u_t. The two visual rays $L(u_{t-1})$ and $L(u_t)$ are shown as parallel vertical lines. The active edge list consists of edges $E_1, \ldots, E_6$, in that order. Edges with odd (resp. even) indices are front (resp. back). At this stage, the algorithm triangulates the cells between edge pairs (E_1, E_2), (E_3, E_4), and (E_5, E_6).

some arbitrary parameter value u_0 and "stretching" it on a plane so that the visual rays turn into vertical lines and the contour parameter u increases from left to right (Figure 16). In the horizontal direction, all edge points of the cone strip are kept sorted by their u-coordinates. In the vertical direction, the edge points are sorted according to an oriented projective *linear ordering*. The precise definition of this ordering will be given in Section 4.3.1, but for now, we can think of it as sorting all the points that intersect the same visual ray according to their distance from the ith camera center (because of our commitment to the oriented projective framework, we cannot use metric depth or distance values directly).

The two key data structures maintained by the triangulation algorithm are an *event list* and an *active list*. The event list gives the discrete set of u-coordinates through which the sweeping ray passes in the course of the algorithm. These coordinates, sorted in the increasing order of u, correspond to the endpoints of all the strip edges. The active list, updated at each successive event value, is a list of edges that intersect the sweeping ray at its current location. If the ray passes the first endpoint of an edge, that edge is inserted into the active list, and if the ray passes the second endpoint of an edge already in the list, that edge is deleted. The edges in the active list are kept sorted according to their linear order along the sweeping ray. In addition, they are also labeled by their *front/back status*. This status, which will be formally defined in Section 4.3.1, describes the relative location of the edges with respect to the strip interior. Namely, between any two consecutive event locations u_{t-1} and u_t, the boundary of the cone strip decomposes into pairs of front/back edges that bound pieces of the cone strip, or *cells*, in their interior. For example, in Figure 16, the interior of the strip is bounded between edge pairs (E_1, E_2), (E_3, E_4), and (E_5, E_6). These cells are *monotone*, i.e., they intersect the sweeping ray along at most a single interval. They are triangulated using a simple linear-time algorithm for monotone polygons (O'Rourke, 1998). This step is completely standard, and we omit its

details in our presentation. In practice, the triangles obtained by this procedure are very long and thin, and require remeshing (see Section 5.4 for details).

4.3.1. *Linear Ordering and Front/Back Status*

In the remaining part of this section, we complete the specification of the triangulation algorithm by supplying the definitions of linear ordering and front/back status. We first define these notions for individual points where the sweeping ray intersects a cone strip, and then extend them to entire edges of the cone strip.

Let X and Y be two distinct points on the visual ray L_i. We can define a linear ordering relation "$<$" on these points as follows:

$$X < Y \quad \text{iff} \quad L_i \simeq X \vee Y \,.$$

It is possible to compute this ordering in an image-based fashion by looking at the projections of the points X and Y into some other view j. The visual ray L_i projects onto the epipolar line $l_{ji} = \mathcal{F}_{ij} x_i$, while X and Y project onto points $x_j = \mathcal{P}_j X$ and $y_j = \mathcal{P}_j Y$. The projection preserves the relative orientation of X and Y, so we have

$$L_i \simeq X \vee Y \quad \text{iff} \quad l_{ji} \simeq x_j \vee y_j \,. \tag{5}$$

The notion of linear ordering can be easily extended from individual points lying on a visual ray to two edges of a cone strip that are intersected by the same visual ray. Let E and E' denote two edges of the ith cone strip and L_i be any ray touching these edges in two distinct points X and Y. Because of the way we construct strip edges, E and E' cannot intersect in their interior (at most, they can share an endpoint). Therefore, the relative ordering of X and Y will remain the same for any ray L_i that intersects both E and E', and we can say that $E < E'$ if and only if $X < Y$ for some particular choice of the two points.

In order to insert a new edge into the active list, we must locate its proper position with respect to the existing active edges. Since the active list is kept sorted, we can locate the new edge using a binary search that involves a series of comparisons against individual active edges. Let E denote an active edge, and

suppose that the current event location u_t corresponds to Y, the first endpoint of of a new edge E'. Let us describe how to test the linear order of E and E' (Figure 17). First, we find the intersection of the existing edge E with the sweeping ray $L_i(u_t)$. Specifically, suppose that E is a segment of the intersection curve I_{ij} of the ith and jth cones. Recall that the image-based representation of E produced by the tracing algorithm of Section 4.1.2 consists of a piecewise-linear chain of (u, v) pairs, where v is the parameter value of the jth contour. So, we simply find the value v_t corresponding to u_t in the description of E (using interpolation, if necessary). The point $x_j(v_t)$ on the jth contour is the projection of the point X where the sweeping ray $L_i(u_t)$ intersects E. Then we can use the image-based formula (5) to test the relative ordering of x_j and $y_j = \mathcal{P}_j Y$, which, in turn, will give us the relative ordering of E and E'.

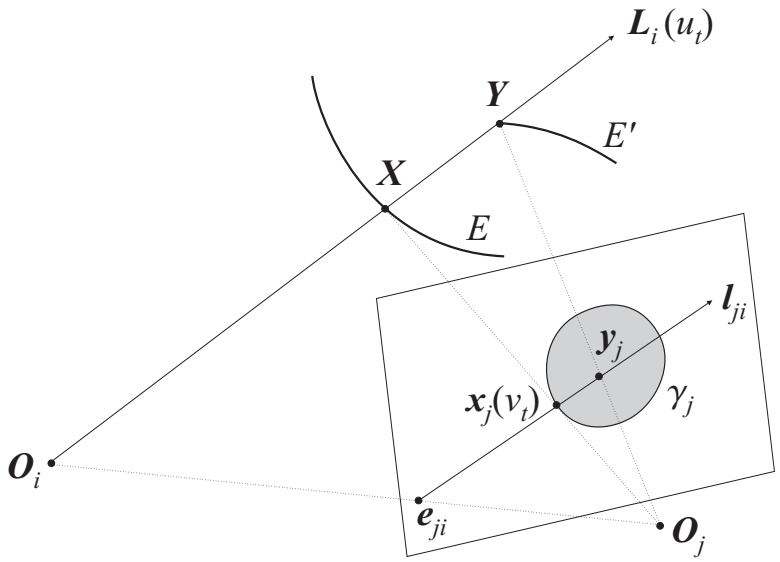

Figure 17. Testing the relative order of an edge E already in the active list and edge E' that is being inserted (see text).

Some updates of the active list involve the simultaneous insertion of two edges that share the same first endpoint (for example, edges E_1 and E_2 in Figure 16). In these cases, simply locating the shared endpoint in the active list is not sufficient to determine which of the two edges should come first. We solve this problem

by selecting a value of u that falls in the interior of both edges, constructing the points where they meet the ray $L_i(u)$, and testing the relative orientation of these two points.

Next, let us define the *front/back* classification of intersection curve points bounding the cone strip. Let X be a point on the boundary of the ith cone strip, and L_i be the visual ray passing through X. X is said to be a *front* (resp. *back*) point with respect to the ith view if it is the first (resp. last) point of the interval on L_i that lies on the visual hull and has X as an endpoint. That is, for any point Y in the interior of this interval, we have $X < Y$ (resp. $X > Y$). The following proposition, whose proof is given in Appendix D.3, yields a convenient image-based criterion for determining the front/back status of X (Figure 18):

Proposition 3. *Suppose that X is a point on the 1-skeleton of the visual hull that belongs to the intersection curve I_{ij}. Then X is a front (resp. back) point on the boundary of the ith cone strip if and only if $t_j \vee e_{ji} < 0$ (resp. > 0), where t_j is the tangent to γ_j at the point $x_j = \mathcal{P}_j X$.*

Notice that the sign of $t_j \vee e_{ji}$ can only change at a frontier point. Since the edges of the 1-skeleton cannot contain frontier points in their interior, the front/back status is actually the same for all points in the interior of a single edge of the 1-skeleton. Thus, just as with linear ordering, we can extend the definition of front/back status to apply to entire edges. Namely, an edge E of the 1-skeleton, considered as part of the boundary of the ith cone strip, is called *front* (resp. *back*) if each point in its interior is a front (resp. back) point.

In the course of the triangulation algorithm, we have to test the front/back status of an edge when it is inserted into the active list. This is done by applying the test of Proposition 3 to its first endpoint X, provided that X is not a type 3A critical point. In the latter case, the projection x_j of X in the jth view is a frontier point, and the test fails because $t_j \vee e_{ji} = 0$. In principle, it is still possible to determine the front/back status of the edge using only local information, based on the behavior of the first and second derivatives of the

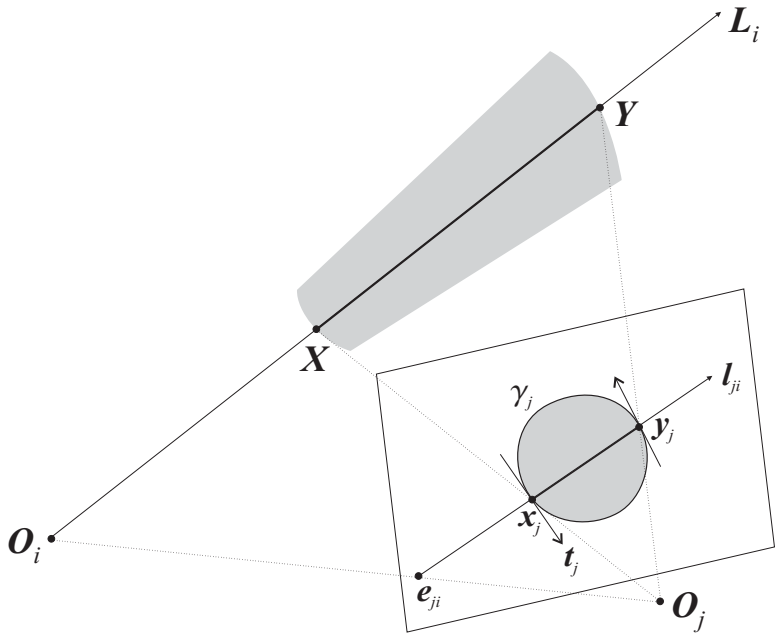

Figure 18. Front/back status of points on visual rays. X is a front point of the bold interval on the ray L_i because $t_j \vee e_{ji} < 0$ (the positive orientation of the image plane is counterclockwise). Y is a back point.

jth contour at x_j (Lazebnik, 2002). We omit the details of this analysis in the current presentation, since a more robust and straightforward solution to the same problem is simply to test another point in the interior of the edge.

5. Implementation Details

We have implemented the proposed approach in C++. This section discusses implementation issues that have not been addressed so far in this article.

5.1. Discrete Contour Representation

In describing our algorithms in Section 4, we have assumed a continuous contour representation. In the implementation, however, contours are piecewise-linear. Therefore, we now need to give discrete definitions of frontier points and alternative formulas for computing their types.

A frontier point on a piecewise-linear contour is a vertex whose two incident edges have different relative orientations with respect to the epipole. This definition is illustrated in Figure 19, left, where x_i is a vertex and t_i^- and t_i^+ are the two contour "tangents"—that is, the properly oriented lines containing the two edges preceding and following x_i along the contour orientation, respectively. Then the necessary and sufficient condition for x_i being a frontier point can be written as

$$t_i^- \vee e_{ij} \simeq -t_i^+ \vee e_{ij} \, .$$

Notice that we are making the general position assumption that the epipole does not lie on either t_i^- or t_i^+. In practice, we have found this assumption to be justified, since noise and errors in contour extraction and calibration effectively "perturb" all the data points, thereby eliminating degeneracies.

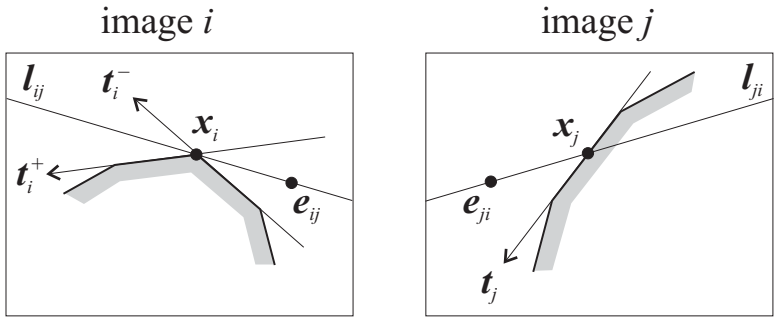

Figure 19. Discrete computation of critical points and their types (see text).

Next, we need to give a discrete analogue of Proposition 2, which is necessary for determining critical point types during tracing of intersection curves. Since we cannot directly compute the differential quantities f_v and f_{uu} used in this proposition, we will fall back on their geometric interpretations. Recall that the sign of f_{uu} tells us about the change of the relative orientation of the contour tangent and the epipole. Namely, when $f_{uu} > 0$, the epipole migrates from the negative to the positive side of the tangent, and when $f_{uu} < 0$, it migrates from the positive side to the negative. This reasoning directly translates to the

following discrete rule:

$$f_{uu} > 0 \quad \Longleftrightarrow \quad t_i^- \vee e_{ij} < 0 \;\text{ and }\; t_i^+ \vee e_{ij} > 0\,,$$
$$f_{uu} < 0 \quad \Longleftrightarrow \quad t_i^- \vee e_{ij} > 0 \;\text{ and }\; t_i^+ \vee e_{ij} < 0\,.$$

For example, in Figure 19, $f_{uu} > 0$ at x_i. The other important quantity used in Proposition 2 is $f_v = t_j \vee e_{ji}$. It is also used in Proposition 3 to determine the front/back status of a point of the 1-skeleton using purely image-based information. To compute $t_j \vee e_{ji}$ in the discrete case, we simply define t_j as the properly oriented line supporting the edge of the jth contour that contains x_j, the point of intersection of the contour and the epipolar line l_{ji} (Figure 19, right). Note that by our general position assumption, x_j cannot be a vertex. In the figure, we have $t_j \vee e_{ji} < 0$ at x_j.

5.2. Computational efficiency: Clipping intersection curves

Most of the processing time of our visual hull construction algorithm is spent on two basic operations, curve/line and curve/curve intersections. These operations are performed during tracing of intersection curves and clipping of reprojected intersection curves against image contours, respectively. Recall from Section 4.1.2 that most line-contour intersections performed by our algorithm are incremental—that is, the line is moved by a small offset, and the new intersection is found by searching in the neighborhood of the previous one. Effectively, this approach finds each new intersection in constant time, so this operation is not a major source of inefficiency for our algorithm. Thus, the main computational bottleneck for our approach is clipping the projection ι_{ij}^k of an intersection curve I_{ij} against an image contour γ_k. In the implementation, ι_{ij}^k and γ_k are both piecewise linear, and the clipping procedure reduces to a sequence of intersection checks between each line segment of ι_{ij}^k and the contour γ_k. Next, let us describe the data structures that we use to perform these checks efficiently (Figure 20, (a)-(c)). In order to make the implementation as simple as possible, we subdivide

ι_{ij}^k to make sure that its every segment has length of at most one pixel in the image.

The first data structure is a bitmap B_k, whose resolution is the same as that of the kth input image. $B_k(x, y)$ is set to 1 if γ_k passes through the corresponding pixel, and 0 otherwise. Note that the bitmap contains 0 in most of the pixels. Then, if a line segment covers only empty pixels, we can tell in time proportional to the segment's image length that there are no intersections. In our case, since the length of all segments is bounded above by a pixel, this check effectively takes constant time. The second data structure is an array of C bins $G_k^c (c = 1, \ldots, C)$, where each bin stores a subset of the line segments forming the contour γ_k. More concretely, suppose the height of the kth image is Y_k, then the bin G_k^c stores the set of line segments whose corresponding y-intervals intersect with the range $[Y_k \frac{c-1}{C}, Y_k \frac{c}{C}]$. Note that a single line segment can be stored in multiple bins. For example, in Figure 20 (c), red, green, and blue line segments are stored in G_k^1, G_k^2, and G_k^3, respectively. We let $C = 15$ throughout our experiments, while for the purpose of illustration, $C = 3$ in Figure 20 (c). With the help of the above two data structures, the intersection check between a line segment s and the image contour γ_k is performed as follows: If $B_k(x, y) = 0$ for all the pixels which s passes through, report *no intersection* (the fast check), otherwise compute intersection(s) of s with all the line segments stored in the bins whose corresponding y-intervals intersect with that of s (the slow check). Note that since our implementation guarantees that s is less than one pixel in length, there must exist at least one interval that fully contains s.

Let M and N denote the numbers of line segments in ι_{ij}^k and γ_k, respectively, and P denote the number of intersections between these curves. In theory, we have $P = O(MN)$. For typical datasets, however, it is reasonable to assume that P is bounded above by a constant smaller than M and N. Furthermore, most of the segments forming ι_{ij}^k require only a constant-time fast check against γ_k, while the number of segments that require slow checks is on the order of P.

Under these assumptions, since the worst-case cost of a slow check is linear in N (and is in fact accelerated by a significant constant using our multi-bin data structure), the running time of the algorithm is thus $O(M + NP)$. In practice, this results in a significant improvement over the brute-force implementation that exhaustively intersects each segment of ι_{ij}^k with each segment of γ_k and thus has complexity $O(MN)$.

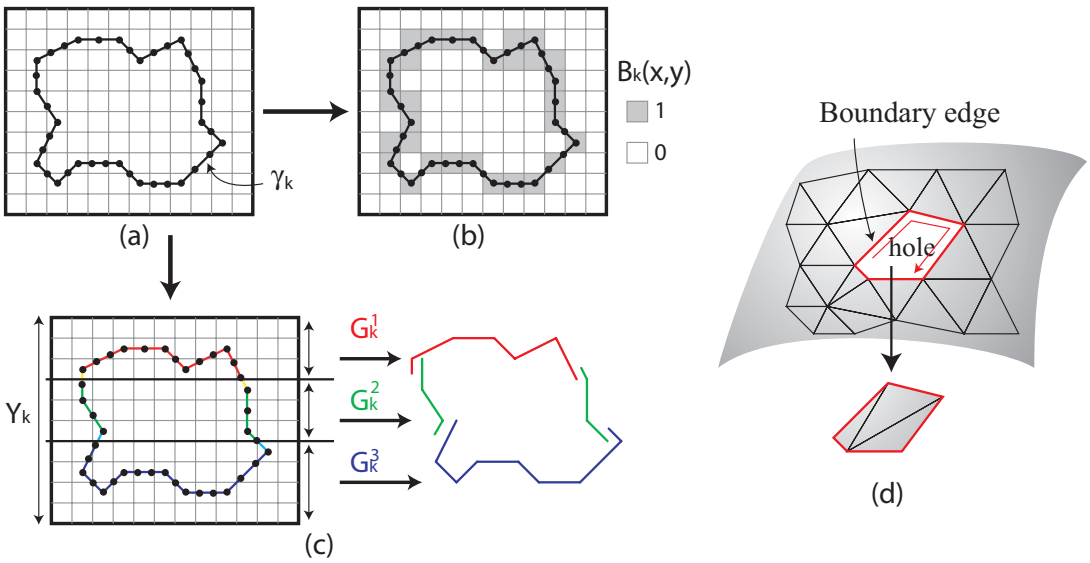

Figure 20. Implementation details. Efficient implementation of the clipping procedure: (a) Given an image contour γ_k, we build two additional data structures: (b) A bitmap $B_k(x, y)$, and (c) A set of bins G_k^c storing line segments in γ_k (see text for details). (d) Due to failures in identifying triple intersection points, our outputs may contain holes. To fill them, we first identify boundary edges where a face is defined only on one side. Then, we trace the boundaries, identify loops, and triangulate them to fill holes.

5.3. Identifying intersection points

As explained in Section 4.2, every time a new image is added in our incremental construction algorithm outlined in Figure 5, we obtain a set of triple intersection points that need to be identified. Each point is associated with three images: the pair of images used to generate an intersection curve and the third image used to clip it. For each triple of images, we collect the corresponding intersection points, and perform the following greedy identification procedure. Let X_1, X_2 and X_3 be three intersection points associated with images i, j, and k, with corresponding

contour parameter values (u_1, v_1, w_1), (u_2, v_2, w_2), and (u_3, v_3, w_3). Then the cost function for identifying this triple is

$$\sum_{(l,m) \in \{(1,2),(1,3),(2,3)\}} |u_l - u_m| + |v_l - v_m| + |w_l - w_m| .$$

Triples of intersection points are identified using the following greedy algorithm:

1. Collect all intersection points associated with the same triple of images.
2. Find the triple from this set with the minimum identification cost.
3. If the cost is less than a pre-determined threshold μ, identify the three points, remove them from the set and go back to the second step; otherwise, terminate the procedure.

We set μ to 0.05 times the average image contour length in all our experiments.

In the results presented in Section 6, not all triples of intersection points are successfully identified. In fact, as shown by Table I in the next section, up to 6% of intersection points can be left unmatched. However, these mistakes of the identification process are not due to our greedy matching procedure, but to the fact that the positions of the intersection points are not always precisely estimated during the clipping procedure because of numerical inaccuracies of the transfer (reprojection) procedure. It is also important to point out that in practice, unmatched intersection points cause only small inconsistencies in the structure of the computed visual hull model, and are easily repaired using the hole-filling algorithm described next.

5.4. Hole filling and remeshing

Due to failures in identifying triple intersection points, cone strips formed by the intersection curves may not be closed and may miss some of their boundaries. As a result, the output of the triangulation algorithm described in Figure 15 may contain holes where edges are missing. To fill those holes, we use a simple boundary traversal algorithm (Figure 20(d)). Given a polygonal mesh, we first

identify its *boundary edges*, where a face is defined on only one side, then trace boundary edges to identify a loop, and finally trianglulate the loop to fill the hole. Although it is a very simple procedure, holes have been successfully filled at all the boundary edges in all our experiments. See Section 6.3 for a discussion of topological consistency of the output.

The final implementation issue is remeshing. Recall from Section 4.3 that the mesh produced by our strip triangulation algorithm lacks vertices in the interiors of cone strips, and its triangles tend to be rather long and thin. However, image-based modeling approaches that use the visual hull mesh to initialize multiview stereo optimization, e.g., (Furukawa and Ponce, 2006), typically require meshes with more uniformly sampled vertices, and triangles that have a better aspect ratio. To obtain a higher-quality mesh for subsequent processing, we can perform an optional remeshing step consisting of a sequence of edge splits, collapses, and swaps (see (Hoppe et al., 1993) for details of these operations). Briefly, edge splitting is performed for edges that are too long, edge collapsing is performed for edges that are too short, and edge swapping is performed to make sure that the degree of each vertex is close to six, thus yielding a more regular triangulation. This process is constrained to make sure that important visual hull structures are preserved: Namely, edge swaps and collapses are not performed if the operation involves an edge that belongs to an intersection curve, i.e., an edge on the boundary of two cone strips. Note that we perform remeshing only when the visual hull mesh is required as input for further processing. In particular, all the running times and mesh sizes reported in the next section are not affected by remeshing.

6. Experimental Results

This section demonstrates the effectiveness of our visual hull algorithm by presenting results on several challenging datasets and conducting a comparative

`skull`: 24 images
1900 × 1800

`dinosaur`: 24 images
2000 × 1500

`alien`: 24 images
1600 × 1600

`predator`: 24 images
1800 × 1700

`roman`: 48 images
3500 × 2300

Figure 21. A sample input image from each dataset, with the total number of images in the dataset and the approximate object size, i.e., the average size (in pixels) of the object's approximate bounding boxes in all the input images. These datasets are available online at `http://www-cvr.ai.uiuc.edu/ponce_grp/data/visual_hull`.

evaluation with another state-of-the-art method, the *exact polyhedral visual hull* of Franco and Boyer (2003).

6.1. Data Acquisition

In addition to the `gourd` sequence used as a working example in Section 4, we have tested the proposed method on five real objects with complex 3D geometry: `skull`, `dinosaur`, `predator`, `roman`, and `alien` (Figure 21). These datasets have been acquired using a motorized turntable and three Canon EOS 1D Mark II cameras equipped with f1.4 50mm lenses. The cameras are calibrated using Intel's OpenCV package,[7] except for the `roman` dataset, which is calibrated using

[7] The library is available at `http://www.intel.com/technology/computing/opencv`.

Table I. Basic statistics of computed visual hull models. First three columns list the numbers of critical points, identified intersection points, and unidentified intersection points for each dataset. The fourth column lists the running time of our algorithm on an Intel Pentium IV desktop machine with a 3.4GHz processor and 3GB of RAM. The first number is the time to build the 1-skeleton, and the second number is the time to triangulate cone strips and fill holes. The overall running time is the sum of the two.

Dataset	# critical pts.	# identified intersection pts.	# unidentified intersection pts.	time (s)
`skull`	6,684	8,004	122	318.9 + 76.8
`dinosaur`	2,889	11,190	660	415.7 + 97.7
`alien`	1,168	9,052	602	478.6 + 53.7
`predator`	2,682	11,223	663	573.2 + 164.0
`roman`	10,840	32,319	1,697	4,051.3 + 1,154.3

the package of Lavest et al. (1998). It is important to note that, even though we use strong calibration for convenience purposes, we do not actually rely on any metric information in the process of computing the visual hulls.

We follow a semi-automatic procedure to extract outlines from the raw images. First, we manually segment foreground pixels using Adobe PhotoShop and obtain discretized contours by traversing the boundary of the foreground pixels. Next, we smooth the contours and resample them to make sure that successive vertices are less than one pixel apart. Finally, we orient the contours to observe the convention described in Section 3.2. In particular, this means that the orientation of the holes is opposite of that of the outer contour. All the datasets used in this section, including the original input images, camera calibration parameters, and extracted contours, are publicly available at `http://www-cvr.ai.uiuc.edu/ponce_grp/data/visual_hull`.

6.2. Computed Visual Hulls

This section presents results of our proposed visual hull computation algorithm applied to the five objects from Figure 21. Figure 22 shows visual hull models of each object from four different viewpoints. Table I gives basic statistics for each model, including the numbers of critical points and identified/unidentified intersection points generated during the procedure. Even though up to 6% of intersection points are left unidentified, high-quality visual hull models are obtained with the help of the hole-filling procedure described in Section 5.4. The last two columns of Table I show the running times of the two stages of our algorithm, namely, building the 1-skeleton and triangulating the cone strips.

Recall that our visual hull construction algorithm (Figure 5) is incremental, i.e., it builds the visual hull by successively adding images one by one and updating the model. Accordingly, Figure 23 illustrates how the visual hull is refined as more input images are added. Finally, Figure 24 shows visual hull models with textures from the original input images mapped onto their surfaces.

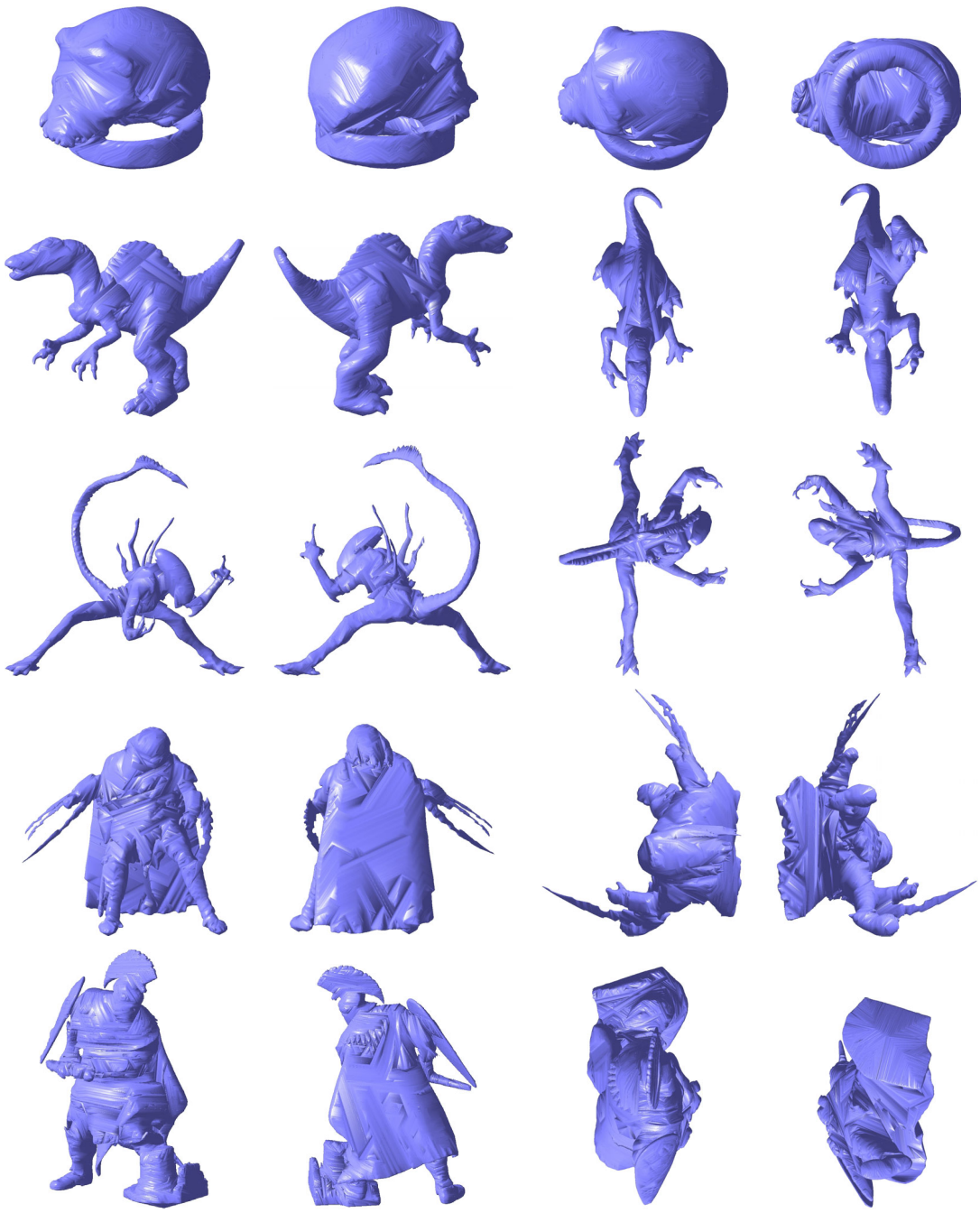

Figure 22. Computed visual hull models for each dataset as seen from four different viewpoints.

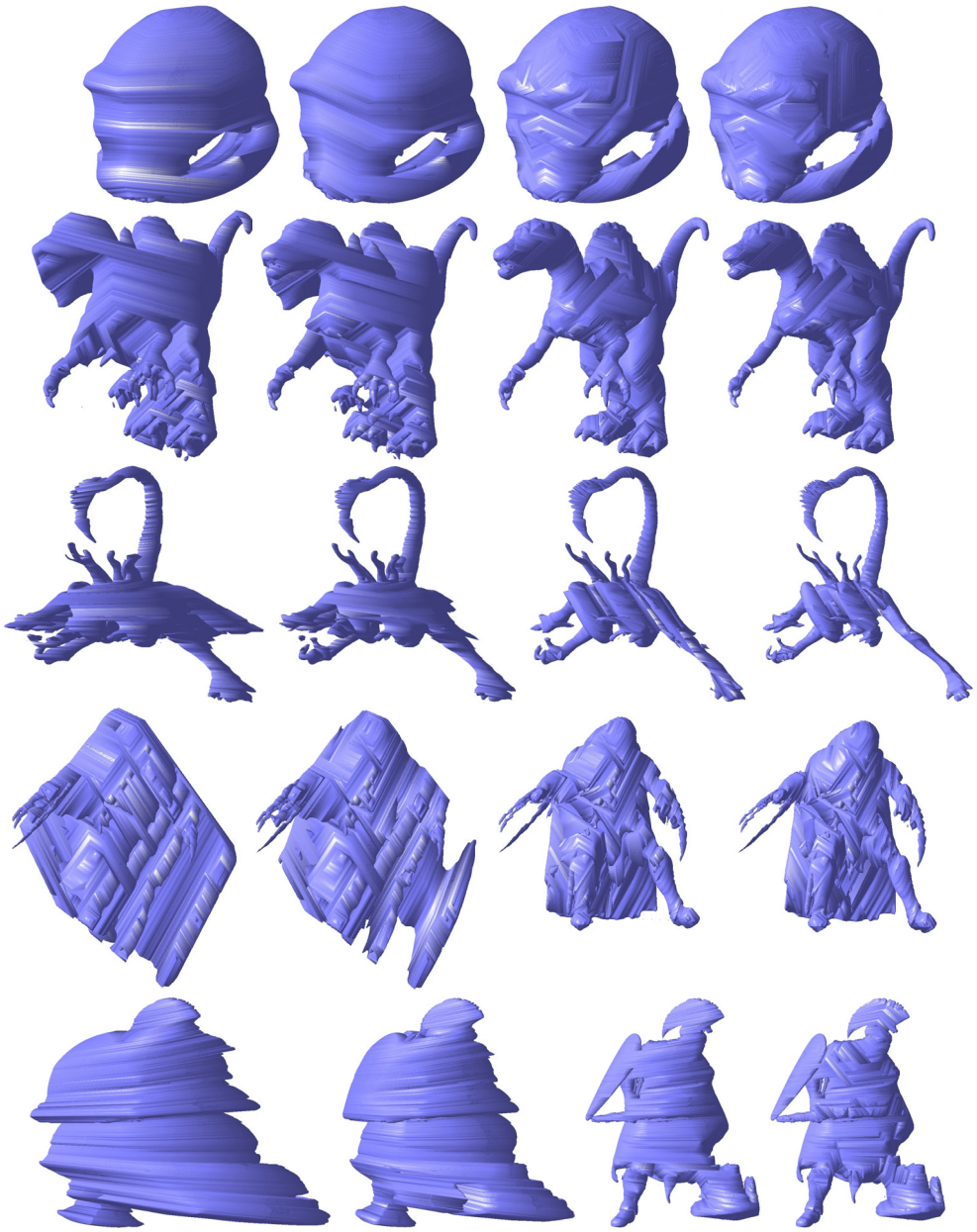

Figure 23. Incremental refinement of visual hull models. From left to right, subsets of 3, 4, 8, and 12 images, respectively, are used to build the visual hull for each object.

Figure 24. Texture-mapped models. Each face (triangle) on the mesh is mapped with texture from the image whose corresponding optical axis has the smallest angle from the face normal orientation. This is obviously not a projective criterion, but we must emphasize that it is used for visualization purposes only, as texture-mapping is not part of the original visual hull construction algorithm.

6.3. Comparative Evaluation

This section presents a comparison between the method proposed in this article and the *exact polyhedral visual hull* algorithm (EPVH) (Franco and Boyer, 2003; Franco, 2005). EPVH is a state-of-the-art recent algorithm that has been explicitly designed to be robust and computationally efficient. The strategy employed by EPVH is, in a sense, complementary to ours: Whereas our algorithm first computes the 1-skeleton and then fills in the interiors of the cone strips, EPVH begins by computing the *viewing edges*, or intervals on visual rays that lie in the interiors of the cone strips, and then fills in the intersection curve segments and triple points that connect these edges. Unlike our algorithm, which has to match triple occurrences of the same intersection points, EPVH finds each intersection point exactly once. Finally, unlike our algorithm, which computes

many intermediate structures that do not belong to the final visual hull (i.e., subsets of intersection curves that later get clipped out), EPVH computes the final visual hull surface in a non-incremental fashion.

Table II shows a comparison between our method and EPVH versions 1.0 and 1.1. These two versions have complexity $O(n^2\,p^2)$ and $O(n^2\,p\log p)$, respectively, where n is the number of views and p is the average number of segments on each image contour (Franco, 2005). Note that EPVH 1.1 has only become available to us close to press time, and is more recent than our own implementation. To make sure that the outputs and running times are exactly comparable, we have used the same sets of piecewise-linear contours as inputs to all the algorithms. The first two columns of Table II show the numbers of vertices (N_v) and faces (N_f) of the visual hull models computed by each method. We can see that our models are somewhat larger in terms of the number of vertices and faces. We have verified that the polygonal meshes constructed by all algorithms are manifolds by checking two conditions: (1) Every edge is incident to exactly two faces; and (2) the link of every vertex is a triagulation of the circle (Hoffmann, 1989). The meshes output by all algorithms satisfy these two conditions for all the data sets. The third column of Table II shows the genus G of the models computed using the Euler-Poincaré formula (Hoffmann, 1989): $N_v - N_e + N_f - 2(1 - G) = 0$, where N_e is the number of edges (not shown in the table).[8] Note that the genera of the models produced by our method and EPVH are different for most of the datasets. Even though the genus of the visual hull is often different from that of the original object and the correct number is unknown, our algorithm seems to produce extraneous small handles due to mistakes in identifying triple intersection points and the subsequent hole-filling procedure. By contrast, the models output by both versions of EPVH have fewer topological imperfections because EPVH explicitly handles intersection points by iteratively

[8] Note that the visual hulls for our data typically consist of multiple connected components, the largest one containing the target object and several smaller ones not corresponding to any actual object structure. Therefore, we discard these smaller components and compute all the numbers (N_v, N_e, N_f, G) only for the largest connected component.

generating missing points to remove inconsistencies (Franco and Boyer, 2003). However, except for unmatched intersection points, which may cause microscopic differences, the structure of the models produced by our method and EPVH looks identical down to very small-scale detail, as shown in Figure 25.

Table II. Comparison of our method and two versions of EPVH. The numbers of vertices (N_v) and triangles (N_f), and the genus of the largest connected component of the visual hull model are shown for our method and EPVH 1.0 and 1.1. The fourth column shows the running times of all three algorithms, reported for an Intel Pentium IV desktop machine with a 3.4GHz processor and 3GB of RAM.

Dataset	method	# vertices	# faces	genus	time (s)
`skull`	ours	486,480	972,984	7	395.7
	EPVH 1.0	401,832	803,684	6	5,614.4
	EPVH 1.1	401,830	803,680	6	128.9
`dinosaur`	ours	337,828	675,664	3	513.4
	EPVH 1.0	290,452	580,900	0	6,329.5
	EPVH 1.1	290,456	580,908	0	138.0
`alien`	ours	209,885	419,770	1	532.3
	EPVH 1.0	171,752	343,500	0	3,362.9
	EPVH 1.1	171,752	343,500	0	119.3
`predator`	ours	375,345	750,806	30	737.2
	EPVH 1.0	306,152	612,420	30	5,078.2
	EPVH 1.1	306,152	612,420	30	136.0
`roman`	ours	1,258,346	2,516,764	19	5,205.6
	EPVH 1.0	884,766	1,769,576	12	53,862.0
	EPVH 1.1	884,750	1,769,544	12	2,147.4

The last column of Table II shows the running times of all three algorithms. Note that our running time is the sum of the two numbers in the last column of Table I. We can observe that our method runs from six to ten times faster than EPVH 1.0, but two to five times slower than EPVH 1.1. A more complete picture can be obtained by investigating how the performance of the different methods scales with the size of the input. Accordingly, Figure 26 shows running times for the three algorithms obtained by uniformly sampling image contours at three different resolutions. Since our algorithm requires each contour segment to be less than one pixel long, in addition to sub-sampling contour segments,

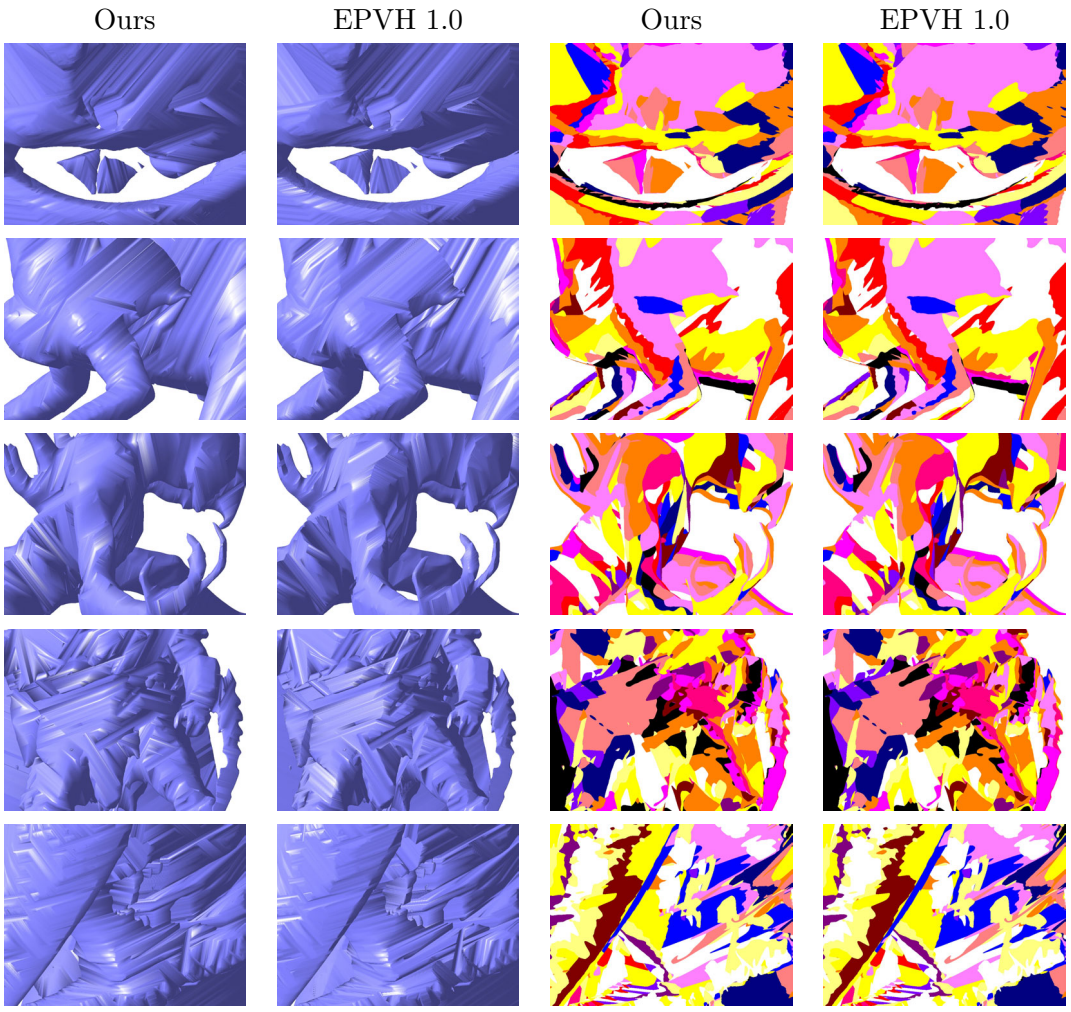

Figure 25. Detailed comparison of the visual hull models reconstructed by our method and EPVH 1.0 (note that the outputs of EPVH 1.0 and 1.1 are exactly the same in most cases). First and second columns: closeups of shaded models. Third and fourth columns: closeups of color-coded models, where cone strips associated with different images are indicated by different colors.

we have multiplied their image coordinates by the sampling ratio. As Figure 26 shows, for every doubling of the contour resolution, the running time of EPVH 1.0 approximately quadruples, while the performance of our algorithm and of EPVH 1.1 scales much better with input size. Unlike Franco and Boyer (Franco and Boyer, 2003), we cannot give a simple expression for the asymptotic running time of our algorithm since it depends in non-trivial ways on the geometric complexity of the input object and of the silhouettes (for example, the time for computing an intersection curve depends on the number of critical points, and

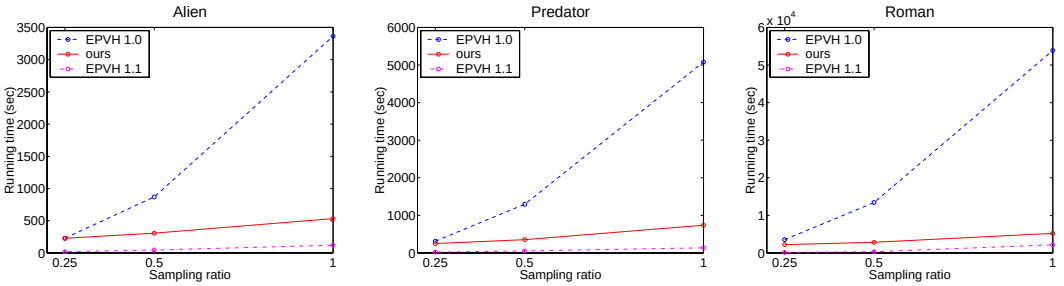

Figure 26. Comparison of our method with EPVH 1.0 and 1.1 for three datasets (alien, predator, roman). The figure shows how the running times of the three algorithms change as we uniformly sub-sample the input image contours. Note that the complexity of the corresponding models (the numbers of vertices and faces) scales approximately linearly for all methods, with EPVH 1.0 and 1.1 producing smaller models than our algorithm, as can be seen from Table II.

the time for clipping this curve depends on the number of its intersections with the silhouette). Nevertheless, based on our comparative evaluation of scaling behavior, we conjecture that the asymptotic running time of our algorithm is close to that of EPVH 1.1, but with larger constants to account for some inefficiencies in our current implementation. In particular, our algorithm spends time on computations that are in principle unnecessary, such as computing parts of intersection curves that are later clipped away. In the future, we plan to develop an improved "hybrid" algorithm that would be like our current method in relying exclusively on image-based oriented projective constructions, and like EPVH in avoiding redundant computations and topological inconsistencies.

7. Discussion

This article has presented an image-based algorithm for computing visual hulls using oriented projective constraints. The following is a summary of our main contributions, both theoretical and practical:

– We characterize the surface of the visual hull in terms of its *intrinsic projective features*, i.e., frontier points, intersection curves, and intersection points.

– We establish a connection between visual hull topology and multi-view geometry. Specifically, we show that frontier points and intersection points, which determine the connectivity of cone strips, are in turn determined by certain kinds of contacts between visual rays and the object's surface (recall Figures 2 and 3).

– We present a complete visual hull construction algorithm that utilizes only *oriented projective constraints* (Lazebnik and Ponce, 2005; Stolfi, 1991). In particular, this algorithm does not require strong calibration, only the knowledge of fundamental matrices for all pairs of cameras in the scene.

– As part of our algorithm, we develop a novel procedure for tracing an intersection curve between a pair of visual cones (Section 4.1.2) that relies on an image-based classification of critical points (Proposition 2) derived from local geometric properties of contours, their tangents, and epipolar lines.

– We demonstrate in Section 6 a practical implementation that works on challenging real-world data and has complexity comparable to that of another state-of-the-art algorithm.

The key target application of our proposed algorithm is *3D photography*, or the acquisition of high-quality 3D models from photographs. In most cases, the visual hull by itself is not a very good approximation to the target shape, since it is required to conform only to the silhouettes in the original pictures. A better approximation is given by a *photo-consistent* shape (Kutulakos and Seitz, 1999) that must exactly reproduce the internal texture patterns seen in the input images of the target object. Accordingly, Furukawa and Ponce (2006) have used the visual hull construction algorithm proposed in this article to build an initial approximation of the object that is subsequently refined using both photo-consistency and silhouette-consistency constraints. Other 3D photography approaches that use the visual hull for initialization include (Hernández Esteban

and Schmitt, 2004; Sinha and Pollefeys, 2005; Sullivan and Ponce, 1998; Vogiatzis et al., 2005).

Appendix

A. Oriented Epipolar Geometry

Let $\mathcal{P}_i$ and $\mathcal{P}_j$ be the properly oriented projection matrices of the ith and jth cameras:

$$\mathcal{P}_i = \begin{pmatrix} P_i^T \\ Q_i^T \\ R_i^T \end{pmatrix}, \qquad \mathcal{P}_j = \begin{pmatrix} P_j^T \\ Q_j^T \\ R_j^T \end{pmatrix}.$$

The knowledge of these camera matrices enables us to compute the properly oriented fundamental matrix $\mathcal{F}_{ij}$ between each pair of views (Lazebnik, 2002):

$$\mathcal{F}_{ij} = \begin{pmatrix} |Q_i, R_i, Q_j, R_j| & |R_i, P_i, Q_j, R_j| & |P_i, Q_i, Q_j, R_j| \\ |Q_i, R_i, R_j, P_j| & |R_i, P_i, R_j, P_j| & |P_i, Q_i, R_j, P_j| \\ |Q_i, R_i, P_j, Q_j| & |R_i, P_i, P_j, Q_j| & |P_i, Q_i, P_j, Q_j| \end{pmatrix}. \tag{6}$$

The properly oriented expressions for the epipoles are as follows:

$$e_{ij} = \begin{pmatrix} |P_i, P_j, Q_j, R_j| \\ |Q_i, P_j, Q_j, R_j| \\ |R_i, P_j, Q_j, R_j| \end{pmatrix}, \qquad e_{ji} = \begin{pmatrix} |P_j, P_i, Q_i, R_i| \\ |Q_j, P_i, Q_i, R_i| \\ |R_j, P_i, Q_i, R_i| \end{pmatrix}.$$

B. Epipolar Consistency

If two points x_i and x_j are the projections of the same 3D point X, then the epipolar constraint $x_j^T \mathcal{F}_{ij} x_i = 0$ is satisfied. Let us now consider the converse of this statement. For example, if we have $x_i \simeq \mathcal{P}_i X$ and $x_j \simeq -\mathcal{P}_j X$, the epipolar constraint is still satisfied, but there is no point in space with a well-defined orientation that would project to the two image points. The following proposition, equivalent to the "strong realizability" condition of Werner and Pajdla (2001b), is proved in (Lazebnik, 2002):

Proposition 4. *Let x_i and x_j be two points that satisfy the epipolar constraint $x_j^T \mathcal{F}_{ij} x_i = 0$ and do not coincide with the respective epipoles e_{ij} and e_{ij}. Then there exists a 3D point X such that $x_i \simeq \mathcal{P}_i X$ and $x_j \simeq \mathcal{P}_j X$ if and only if*

$$\mathcal{F}_{ji} x_j \simeq e_{ij} \vee x_i \quad \text{or equivalently,} \quad \mathcal{F}_{ij} x_i \simeq e_{ji} \vee x_j \,. \tag{7}$$

Next, let us briefly discuss the implications of the epipolar consistency constraint for intersection curve tracing (Section 4.1). The expression (7) can be written as a scalar inequality

$$g(u,v) > 0 \,, \quad \text{where} \quad g(u,v) = \Big(\mathcal{F}_{ij} x_i(u)\Big) \cdot \Big(e_{ji} \vee x_j(v)\Big) \,. \tag{8}$$

It is clear that $g(u,v)$ is a smooth function. Moreover, if we assume that the outlines do not pass through the epipoles, $g(u,v)$ never vanishes whenever $f(u,v) = x_j(v)^T \mathcal{F}_{ij} x_i(u) = 0$. We must conclude that $g(u,v)$ keeps the same sign within a connected component of δ_{ij}, and therefore, within any single branch delimited by critical points. Thus, it is straightforward to identify the parts of δ_{ij} that do not correspond to physical components of the intersection curve in space: Namely, in the first stage of tracing δ_{ij}, when all its vertices (critical points) are identified, it is sufficient to discard all vertices that fail the epipolar consistency test (8).

C. Oriented Epipolar Transfer

Suppose we know two points x_i and x_j in the ith and jth views that are the projections of the same 3D point X. Without explicitly computing X itself, how can we find the properly oriented point $x_k \simeq \mathcal{P}_k X$ in a third view? We can apply the fundamental matrices $\mathcal{F}_{ik}$ and $\mathcal{F}_{jk}$ to map the points x_i and x_j onto their respective epipolar lines in the kth view, $l_{ki} = \mathcal{F}_{ik} x_i$ and $l_{kj} = \mathcal{F}_{jk} x_k$, and then take the intersection of these two lines (Figure 27). However, some extra work needs to be done to ensure orientation consistency (refer to (Lazebnik, 2002) for details). The properly oriented formula for x_k is

$$x_k = \operatorname{sgn}\Big((\mathcal{F}_{ik} x_i) \vee e_{kj}\Big) \Big((\mathcal{F}_{jk} x_j) \wedge (\mathcal{F}_{ik} x_i)\Big) \,, \tag{9}$$

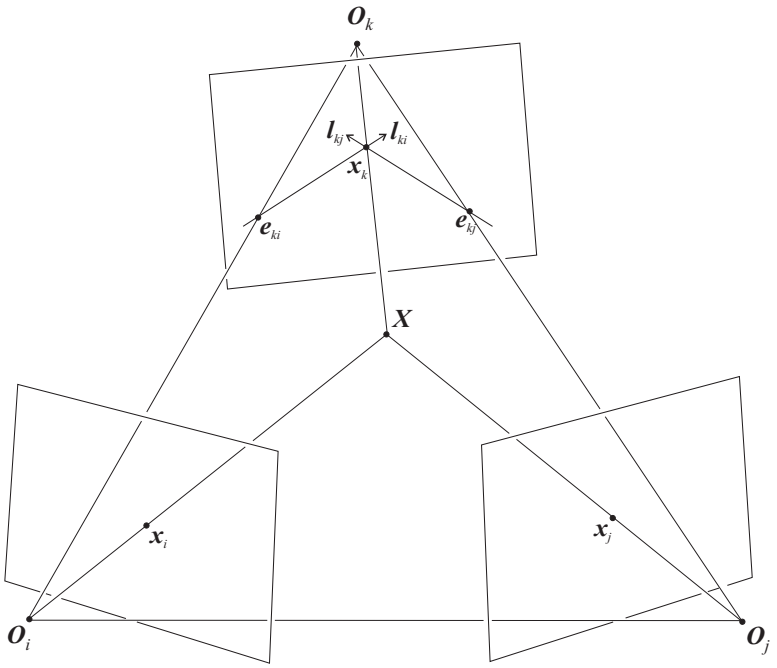

Figure 27. Epipolar transfer (see text).

where the meet of the two lines $\mathcal{F}_{jk}x_j$ and $\mathcal{F}_{ik}x_i$ is given by the cross-product of their coordinate vectors. Though (9) is a simple and convenient formula, it has some pitfalls. In particular, it fails whenever the 3D intersection point X is located in the *trifocal plane* spanned by the camera centers O_i, O_j, and O_k. In practice, the epipolar transfer relationship may become numerically unstable whenever the intersection point lies near the trifocal plane. For this reason, a better implementation choice may be to rely on the more robust transfer procedure based on the trifocal tensor. Deriving this formula is beyond the scope of this article, but refer to (Lazebnik, 2002) for details.

D. Proofs of Propositions 1-3

D.1. Proof of Proposition 1

We would like to find an explicit parametric form for δ_{ij} in the neighborhood of (u_0, v_0). This form is given by a curve $\Big(u(t), v(t)\Big)$ such that $f\Big(u(t), v(t)\Big) \equiv 0$. Assuming that $u_0 = u(t_0)$ and $v_0 = v(t_0)$, Taylor expansion of $f(t) = f\Big(u(t), v(t)\Big)$ about t_0 yields

$$\begin{aligned} f(t_0 + \delta t) &= f(t_0) + f'(t_0)\,\delta t + \frac{1}{2} f''(t_0)\,\delta t^2 + \dots \\ &= f(u_0, v_0) + (f_u\,u' + f_v\,v')\,\delta t + \\ &\quad \frac{1}{2}\Big(f_{uu}\,(u')^2 + 2 f_{uv}\,u'\,v' + f_{vv}\,(v')^2 + f_u\,u'' + f_v\,v''\Big)\,\delta t^2 + \dots \\ &= \frac{1}{2}\Big(f_{uu}\,(u')^2 + 2 f_{uv}\,u'\,v' + f_{vv}\,(v')^2\Big)\,\delta t^2 + \dots . \end{aligned} \tag{10}$$

We obtained (10) by eliminating all terms involving the vanishing quantities $f(u_0, v_0)$, f_u, and f_v. We can further simplify (10) by noticing that the mixed second derivative $f_{uv} = x_j'^T F_{ij} x_i'$ vanishes because the derivative points x_i' and x_j' lie on the respective matching epipolar lines $l_{ij} = F_{ji} x_j$ and $l_{ji} = F_{ij} x_i$. The Taylor expansion of $f(t)$ now becomes

$$f(t_0 + \delta t) = \frac{1}{2}\Big(f_{uu}\,(u')^2 + f_{vv}\,(v')^2\Big)\delta t^2 + \dots .$$

To make sure that $f\Big(u(t), v(t)\Big) \equiv 0$, every coefficient of the Taylor series must be identically zero. In order for the quantity $f_{uu}\,(u')^2 + f_{vv}\,(v')^2$ to vanish, we must have

$$\frac{u'}{v'} = \pm\sqrt{-\frac{f_{vv}}{f_{uu}}}\,.$$

Finally, by finding the expressions for f_{uu} and f_{vv}, it is straightforward to verify that $-\frac{f_{vv}}{f_{uu}}$ is positive (Lazebnik, 2002). The parametric form of a branch of δ_{ij} in the neighborhood of (u_0, v_0) is given by

$$\Big(u(t), v(t)\Big) = (u_0, v_0) + (u', v')t + \dots ,$$

where $(u', v') \simeq \left(\frac{u'}{v'}, 1\right)$ is the tangent vector to the branch. Since $\frac{u'}{v'}$ has two distinct solutions, we must conclude that two distinct curve branches pass through (u_0, v_0), having tangent vectors proportional to $\left(\sqrt{-\frac{f_{vv}}{f_{uu}}}, 1\right)$ and $\left(-\sqrt{-\frac{f_{vv}}{f_{uu}}}, 1\right)$.

D.2. Proof of Proposition 2

Suppose (u_0, v_0) is a type 2 critical point of δ_{ij}: $f_u = 0, f_v \neq 0$. Then in the neighborhood of (u_0, v_0), it is possible to express v as a function of u such that $f\Big(u, v(u)\Big) \equiv 0$. By the second derivative test, the function $v(u)$ has a local maximum (resp. minimum) if $v'' < 0$ (resp. $v'' > 0$). Let us find the expression for v'' by finding the Taylor expansion of $f\Big(u, v(u)\Big)$ about $(u_0, v_0) = (u_0, v(u_0))$:

$$\begin{aligned} f(u_0 + \delta u) \;&=\; f(u_0, v_0) + (f_u + f_v\, v')\delta u + \\ &\qquad \frac{1}{2}\Big(f_{uu} + 2f_{uv}\, v' + f_{vv}\,(v')^2 + f_v\, v''\Big)\delta u^2 + \ldots \qquad (11) \\ &\;=\; \frac{1}{2}\Big(f_{uu} + f_v\, v''\Big)\delta u^2 + \ldots\,. \qquad (12) \end{aligned}$$

In (11), we used the fact that $u' = \frac{\mathrm{d}u}{\mathrm{d}u} = 1$ and $u'' = 0$, and in (12), we eliminated all terms involving the vanishing quantities $f(u_0, v_0)$, f_u, and v' (v' vanishes because the critical point (u_0, v_0) is a local extremum in the v-direction). Because $f\Big(u, v(u)\Big) \equiv 0$, the remaining term $f_{uu} + f_v\, v''$ must also vanish identically. Setting it to zero, we obtain

$$v'' = -\frac{f_{uu}}{f_v}\,.$$

Finally, it is clear that in order to have $v'' < 0$ (resp. $v'' > 0$), the signs of f_{uu} and f_v must be the same (resp. opposite), which proves the first part of the proposition.

If (u_0, v_0) is a type 3 critical point ($f_u \neq 0$, $f_v = 0$), we can use an analogous technique to establish the second part of the proposition. Note that it is possible to show that both f_{uu} and f_{vv} are generically nonzero at critical points of δ_{ij}, thus making sure that critical points of type 2 and 3 cannot be inflections.

D.3. Proof of Proposition 3

Let Y be a point on L_i that is located in the interior of the strip. Then X is a front point if $L_i \simeq X \vee Y$, and is a back point if $L_i \simeq Y \vee X$. Let us consider the information available in the jth view. The visual ray L_i projects onto the epipolar line $l_{ji} = F_{ij}x_i$, while X and Y project onto points x_j and y_j satisfying $l_{ji} \simeq e_{ji} \vee x_j$ and $l_{ji} \simeq e_{ji} \vee y_j$. How can we tell by looking at the projection of X in the jth image whether X is the front or back endpoint of its ray interval? Ideally, we would like an expression that does not include the "fictitious" point y_j. If X is front, then $L_i \simeq X \vee Y$, and $l_{ji} \simeq e_{ji} \vee x_j \simeq x_j \vee y_j$. Therefore,

$$t_j \vee y_j \simeq -t_j \vee e_{ji}\,, \tag{13}$$

where $t_j = x_j \vee x'_j$ is the tangent to γ_j at x_j. By convention, t_j is oriented so that the interior of the silhouette is located on its positive side. Since the interior of the ith cone strip projects into the interior of the silhouette in the jth image, we must have $t_j \vee y_j > 0$. From (13), we can conclude that $t_j \vee e_{ji} < 0$. Similarly, when X is back, we have $t_j \vee e_{ji} > 0$. The above argument can be easily reversed to show that whenever $t_j \vee e_{ji}$ is negative (resp. positive), then X is the front (resp. back) endpoint of its ray interval.

Acknowledgments

This research was partially supported by the UIUC Campus Research Board and by the National Science Foundation under grants IRI-990709, IIS-0308087, and IIS-0312438. The authors would like to thank Jodi Blumenfeld and Steven R. Leigh of the UIUC Anthropology Department for providing the skull, and Jean-Sébastien Franco and Edmond Boyer for making the implementation of their EPVH algorithm publicly available. We are also grateful to Edmond Boyer for providing the gourd data set and for discussions that have led to some of the work presented in this article.

References

Ahuja, N. and J. Veenstra: 1989, 'Generating Octrees from object silhouettes in orthographic views'. *IEEE Trans. Patt. Anal. Mach. Intell.* **11**(2), 137–149.

Arbogast, E. and R. Mohr: 1991, '3D structure inference from image sequences'. *Journal of Pattern Recognition and Artificial Intelligence* **5**(5).

Baumgart, B.: 1974, 'Geometric modeling for computer vision'. Technical Report AIM-249, Stanford University. Ph.D. Thesis. Department of Computer Science.

Bottino, A. and A. Laurentini: 2004, 'The Visual Hull of Smooth Curved Objects'. *IEEE Trans. Patt. Anal. Mach. Intell.* **26**(12), 1622–1632.

Boyer, E. and M.-O. Berger: 1997, '3D Surface Reconstruction Using Occluding Contours'. *Int. J. of Comp. Vision* **22**(3), 219–233.

Boyer, E. and J.-S. Franco: 2003, 'A Hybrid Approach for Computing Visual Hulls of Complex Objects'. In: *Proc. IEEE Conf. Comp. Vision Patt. Recog.*, Vol. 1. pp. 695–701.

Brand, M., K. Kang, and D. B. Cooper: 2004, 'An Algebraic Solution to Visual Hull'. In: *Proc. IEEE Conf. Comp. Vision Patt. Recog.*, Vol. 1. pp. 30–35.

Chum, O., T. Werner, and T. Pajdla: 2003, 'Joint Orientation of Epipoles'. In: *Proc. British Machine Vision Conference*. pp. 73–82.

Cipolla, R., K. Åström, and P. Giblin: 1995, 'Motion from the Frontier of Curved Surfaces'. In: *Proc. Int. Conf. Comp. Vision*. pp. 269–275.

Cipolla, R. and A. Blake: 1992, 'Surface Shape from the Deformation of the Apparent Contour'. *Int. J. of Comp. Vision* **9**(2), 83–112.

Cipolla, R. and P. Giblin: 2000, *Visual Motion of Curves and Surfaces*. Cambridge University Press.

Forsyth, D. and J. Ponce: 2002, *Computer Vision: A Modern Approach*. Prentice-Hall.

Franco, J.-S.: 2005, 'Modélisation tridimensionelle à partir de silhouettes'. Ph.D. thesis, Institut National Polytechnique de Grenoble.

Franco, J.-S. and E. Boyer: 2003, 'Exact Polyhedral Visual Hulls'. In: *British Machine Vision Conference*. pp. 329–338. `http://perception.inrialpes.fr/~Franco/EPVH/index.php`.

Furukawa, Y. and J. Ponce: 2006, 'Carved Visual Hulls for Image-Based Modeling'. In: *Proc. European Conf. Comp. Vision*.

Giblin, P. and R. Weiss: 1987, 'Reconstruction of Surfaces from Profiles'. In: *Proc. Int. Conf. Comp. Vision*. pp. 136–144.

Grauman, K., G. Shakhnarovich, and T. Darrell: 2003, 'A Bayesian Approach to Image-Based Visual Hull Reconstruction'. In: *Proc. IEEE Conf. Comp. Vision Patt. Recog.*, Vol. 1. pp. 187–194.

Grauman, K., G. Shakhnarovich, and T. Darrell: 2004, 'Virtual Visual Hulls: Example-Based 3D Shape Inference from a Single Silhouette'. In: *Proceedings of the 2nd Workshop on Statistical Methods in Video Processing*. MIT AI Memo, AIM-2004-003.

Hartley, R.: 1998, 'Computation of the quadrifocal tensor'. In: *Proc. European Conf. Comp. Vision*. pp. 20–35.

Heo, H.-S., M.-S. Kim, and G. Elber: 1999, 'The Intersection of Two Ruled Surfaces'. *Computer-Aided Design* **31**, 33–50.

Hernández Esteban, C. and F. Schmitt: 2004, 'Silhouette and stereo fusion for 3D object modeling'. *Computer Vision and Image Understanding* **96**(3), 367–392.

Hoffmann, C. M.: 1989, *Geometric and Solid Modeling*. San Mateo, California: Morgan Kaufmann.

Hoppe, H., T. DeRose, T. Duchamp, J. McDonald, and W. Stuetzle: 1993, 'Mesh optimization'. In: *ACM SIGGRAPH*. pp. 19–26.

Koenderink, J.: 1984, 'What does the occluding contour tell us about solid shape?'. *Perception* **13**, 321–330.

Kutulakos, K. and S. Seitz: 1999, 'A Theory of Shape by Space Carving'. In: *Proc. Int. Conf. Comp. Vision*. pp. 307–314.

Laurentini, A.: 1994, 'The Visual Hull Concept for Silhouette-based Image Understanding'. *IEEE Trans. Patt. Anal. Mach. Intell.* **16**(2), 150–162.

Lavest, J.-M., M. Viala, and M. Dhome: 1998, 'Do we really need an accurate calibration pattern to achieve a reliable camera calibration?'. In: *Proc. European Conf. Comp. Vision*. pp. 158–174.

Lazebnik, S.: 2002, 'Projective Visual Hulls'. Master's thesis, University of Illinois at Urbana-Champaign. Also Beckman CVR Technical Report CVR-TR-2002-01, available at `http://www-cvr.ai.uiuc.edu/ponce_grp`.

Lazebnik, S., E. Boyer, and J. Ponce: 2001, 'On Computing Exact Visual Hulls of Solids Bounded by Smooth Surfaces'. In: *Proc. IEEE Conf. Comp. Vision Patt. Recog.* pp. 156–161.

Lazebnik, S. and J. Ponce: 2005, 'The Local Projective Shape of Smooth Surfaces and Their Outlines'. *Int. J. of Comp. Vision* **63**(1), 65–83.

Lorensen, W. and H. Cline: 1987, 'Marching Cubes: A High-Resolution 3D Surface Construction Algorithm'. In: *ACM SIGGRAPH*. pp. 163–170.

Martin, W. and J. Aggarwal: 1983, 'Volumetric description of objects from multiple views'. *IEEE Trans. Patt. Anal. Mach. Intell.* **5**(2), 150–158.

Matsuyama, T., X. Wu, T. Takai, and S. Nobuhara: 2004, 'Real-Time 3D Shape Reconstruction, Dynamic 3D Mesh Deformation, and High Fidelity Visualization for 3D Video'. *Computer Vision and Image Understanding* **96**(3), 393–434.

Matusik, W., C. Buehler, and L. McMillan: 2001, 'Polyhedral Visual Hulls for Real-Time Rendering'. In: *Proc. Twelfth Eurographics Workshop on Rendering*. pp. 115–125.

Matusik, W., C. Buehler, R. Raskar, S. Gortler, and L. McMillan: 2000, 'Image-based Visual Hulls'. In: *ACM SIGGRAPH*. pp. 369–374.

Matusik, W., H. Pfister, A. Ngan, P. Beardsley, R. Ziegler, and L. McMillan: 2002, 'Image-Based 3D Photography Using Opacity Hulls'. In: *ACM SIGGRAPH*. pp. 427–437.

Nistér, D.: 2004, 'Untwisting a projective reconstruction'. *Int. J. of Comp. Vision* **60**(2), 165–183.

O'Rourke, J.: 1998, *Computational Geometry in C*. Cambridge: Cambridge University Press, 2 edition.

Owen, J. and A. Rockwood: 1987, 'Intersection of General Implicit Surfaces'. In: G. Farin (ed.): *Geometric Modeling: Algorithms and Trends*. Philadelphia: SIAM Publications.

Petitjean, S.: 1998, 'A Computational Geometric Approach to Visual Hulls'. *Int. Journal of Computational Geometry and Applications* **8**(4), 407–436.

Porrill, J. and S. Pollard: 1991, 'Curve Matching and Stereo Calibration'. *Image and Vision Computing* **9**(1), 45–50.

Potmesil, M.: 1987, 'Generating octree models of 3D objects from their silhouettes in a sequence of images'. *Computer Vision, Graphics and Image Processing* **40**, 1–29.

Rieger, J.: 1986, 'Three-dimensional motion from fixed points of a deforming profile curve'. *Optics Letters* **11**, 123–125.

Shlyakhter, I., M. Rozenoer, J. Dorsey, and S. Teller: 2001, 'Reconstructing 3D Tree Models from Intrumented Photographs'. *IEEE Computer Graphics and Applications* **21**(3), 53–61.

Sinha, S. and M. Pollefeys: 2004, 'Visual-Hull Reconstruction from Uncalibrated and Unsynchronized Video Streams'. In: *Second International Symposium on 3D Data Processing, Visualization and Transmission*. pp. 349–356.

Sinha, S. and M. Pollefeys: 2005, 'Multi-View Reconstruction Using Photo-consistency and Exact Silhouette Constraints: A Maximum-Flow Formulation'. In: *ICCV*.

Srivastava, S. and N. Ahuja: 1990, 'Octree generation from object silhouettes in perspective views'. *Computer Vision, Graphics and Image Processing* **49**(1), 68–84.

Stolfi, J.: 1991, *Oriented Projective Geometry: A Framework for Geometric Computations*. Academic Press.

Sullivan, S. and J. Ponce: 1998, 'Automatic Model Construction, Pose Estimation, and Object Recognition from Photographs using Triangular Splines'. *IEEE Trans. Patt. Anal. Mach. Intell.* **20**(10), 1091–1096.

Szeliski, R.: 1993, 'Rapid Octree Construction From Image Sequences'. *Computer Vision, Graphics, and Image Processing: Image Understanding* **58**(1), 23–32.

Vaillant, R. and O. Faugeras: 1992, 'Using extremal boundaries for 3D object modeling'. *IEEE Trans. Patt. Anal. Mach. Intell.* **14**(2), 157–173.

Vogiatzis, G., P. H. Torr, and R. Cipolla: 2005, 'Multi-view stereo via Volumetric Graph-cuts'. In: *CVPR*. pp. 391–398.

Werner, T. and T. Pajdla: 2001a, 'Cheirality in Epipolar Geometry'. In: *ICCV*. pp. 548–553.

Werner, T. and T. Pajdla: 2001b, 'Oriented Matching Constraints'. In: *Proc. British Machine Vision Conference*. pp. 441–450.